

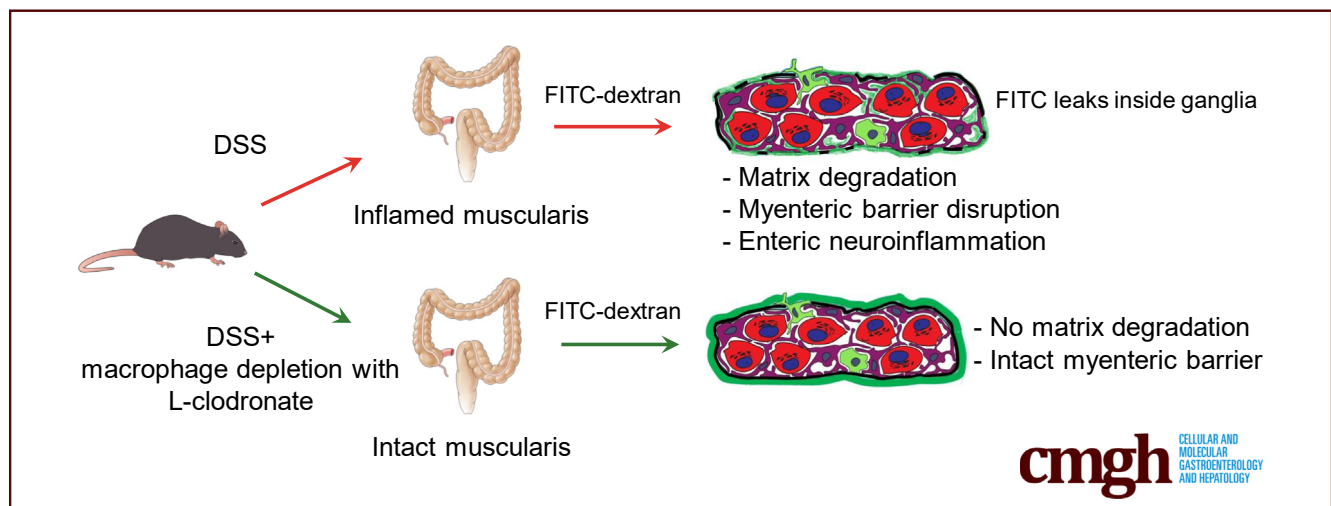
ORIGINAL RESEARCH

Evidence of a Myenteric Plexus Barrier and Its Macrophage-Dependent Degradation During Murine Colitis: Implications in Enteric Neuroinflammation



David Dora,^{1,a} Szilamer Ferenczi,^{2,a} Rhian Stavely,³ Viktoria E. Toth,^{4,5} Zoltan V. Varga,^{4,5} Tamas Kovacs,¹ Ildiko Bodi,¹ Ryo Hotta,³ Krisztina J. Kovacs,² Allan M. Goldstein,³ and Nandor Nagy¹

¹Department of Anatomy, Histology and Embryology, Faculty of Medicine, Semmelweis University, Budapest, Hungary; ²Institute of Experimental Medicine, Laboratory of Molecular Neuroendocrinology, Budapest, Hungary; ³Department of Pediatric Surgery, Massachusetts General Hospital, Harvard Medical School, Boston, Massachusetts; ⁴Department of Pharmacology and Pharmacotherapy, Semmelweis University, Budapest, Hungary; and ⁵HCEMM-SU Cardiometabolic Immunology Research Group, Semmelweis University, Budapest, Hungary



SUMMARY

The impermeable barrier present around the myenteric plexus is disrupted after experimental colitis in a macrophage-dependent manner, exposing enteric neurons and glia to inflammatory cells. This study supports a potential mechanism for the onset of neuroinflammation in colitis and other gastrointestinal pathologies associated with acquired enteric neuronal dysfunction.

BACKGROUND & AIMS: Neuroinflammation in the gut is associated with many gastrointestinal (GI) diseases, including inflammatory bowel disease. In the brain, neuroinflammatory conditions are associated with blood-brain barrier (BBB) disruption and subsequent neuronal injury. We sought to determine whether the enteric nervous system is similarly protected by a physical barrier and whether that barrier is disrupted in colitis.

METHODS: Confocal and electron microscopy were used to characterize myenteric plexus structure, and FITC-dextran

assays were used to assess for presence of a barrier. Colitis was induced with dextran sulfate sodium, with co-administration of liposome-encapsulated clodronate to deplete macrophages.

RESULTS: We identified a blood-myenteric barrier (BMB) consisting of extracellular matrix proteins (agrin and collagen-4) and glial end-feet, reminiscent of the BBB, surrounded by a collagen-rich periganglionic space. The BMB is impermeable to the passive movement of 4 kDa FITC-dextran particles. A population of macrophages is present within enteric ganglia (intraganglionic macrophages [IGMs]) and exhibits a distinct morphology from muscularis macrophages, with extensive cytoplasmic vacuolization and mitochondrial swelling but without signs of apoptosis. IGMs can penetrate the BMB in physiological conditions and establish direct contact with neurons and glia. Dextran sulfate sodium-induced colitis leads to BMB disruption, loss of its barrier integrity, and increased numbers of IGMs in a macrophage-dependent process.

CONCLUSIONS: In intestinal inflammation, macrophage-mediated degradation of the BMB disrupts its physiological barrier function, eliminates the separation of the intra- and extra-ganglionic compartments, and allows inflammatory

stimuli to access the myenteric plexus. This suggests a potential mechanism for the onset of neuroinflammation in colitis and other GI pathologies with acquired enteric neuronal dysfunction. (*Cell Mol Gastroenterol Hepatol* 2021;12:1617–1641; <https://doi.org/10.1016/j.jcmgh.2021.07.003>)

Keywords: Barrier; Enteric Ganglion; Macrophage; ECM; Intraganglionic Macrophage; Colitis.

Among its many essential roles, the gastrointestinal (GI) tract regulates motility, digestion, absorption of nutrients, removal of waste, and protection from pathogens, allergens, and toxins. Many of these functions rely on coordination between the enteric nervous system (ENS) and the immune system. The ENS comprises a complex network of neural and glial cells that is influenced by the central nervous system (CNS) but performs a wide array of functions independently to maintain homeostasis, including regulating GI motility and participating in crosstalk with the microbiota and resident leukocytes of the intestinal immune system.^{1,2} Enteric neuroinflammation disrupts these processes and has been implicated in chronic GI diseases including esophageal achalasia, gastroparesis, chronic intestinal pseudo-obstruction, irritable bowel syndrome, and inflammatory bowel disease (IBD).^{3–6} In IBD, infiltration of nonresident leukocytes to the enteric plexuses (plexitis) is predictive of future relapses, indicating that neuroinflammation may contribute to chronic intestinal inflammation.⁶

Intestinal macrophages are a tissue-specific population of leukocytes descending from erythro-myeloid progenitors that colonize every layer of the gut including the muscularis propria.^{7,8} Whereas mucosal macrophages have a role in antigen sampling and antimicrobial (M1) responses, resident muscularis macrophages (MMs) exhibit an anti-inflammatory (M2) phenotype important in tissue protection and regeneration.⁹ Nevertheless, conditions of inflammation or stimulation by pathogen-associated molecular patterns (PAMPs) can activate resident MMs into a proinflammatory phenotype with unknown consequences on the ENS.^{10,11} Early histologic studies describing ultrastructural features of enteric ganglia^{12–14} identified macrophages closely juxtaposed to nerve fibers¹⁵ and enteric neurons.^{16,17} Recently, subpopulations of microglia-like MMs in proximity to the ENS have been identified, including myenteric plexus macrophages (MyMs), situated in close spatial association with the myenteric plexus,^{18–20} and intraganglionic macrophages (IGMs) in the embryonic and postnatal avian and mouse intestine.²¹ Detailed characterization of the morphology and immunophenotype of MyMs and IGMs has not yet been accomplished. Furthermore, it is unknown whether IGMs and MyMs are the same cell population capable of migrating in and out of the myenteric plexus to interact with enteric neurons and glial cells.

The blood-brain barrier (BBB) of the CNS protects neurons and glia from proinflammatory PAMPs such as lipopolysaccharides (LPS).²² The gut is the major site of interaction between commensal microbiota and the host. Despite some early attempts to characterize the presence of

a “blood-myenteric ganglia” barrier,^{23–25} there is still a gap in our knowledge about the nature of this barrier that might protect enteric neurons and glial cells from exogenous pathogenic macromolecules. During gangliogenesis, migrating enteric neural crest cells secrete extracellular matrix (ECM) molecules, including collagens, tenascin, and agrin.^{26–28} Among these, agrin persists postnatally and could serve to physically separate and protect the enteric ganglia from the surrounding environment.²¹

In the present study, we describe the existence of a barrier that encapsulates the myenteric plexus at an ultrastructural level and consists of ECM proteins and glial endfeet. IGMs are demonstrated to be capable of penetrating the blood-myenteric barrier (BMB) and undergo morphologic transformation. In physiological conditions the BMB is impermeable to fluorescein isothiocyanate (FITC)-dextran, indicating that it is a functional barrier to exogenous macromolecules. Experimental colitis in mice severely disrupts the BMB, degrading its ECM components and disrupting its barrier function. However, this effect can be rescued by the experimental depletion of MMs with L-clodronate, suggesting that inflammation-mediated disruption of the BMB is macrophage-dependent.

Results

A Subset of Hematopoietic Cells in Colonic Enteric Ganglia Possess a Macrophage Signature

We evaluated the presence of IGMs in 1- μ m-thick semithin sections from CX3CR1^{GFP} adult mouse colon labeled with antibody against the ECM protein agrin. Agrin is secreted by neural crest-derived cells²⁸ and demarcates the outer border of the myenteric ganglia.²¹ Green fluorescent protein (GFP) labeling (developed with VectaRed) shows macrophages present inside the enteric ganglia (Figure 1A and B, arrowheads). Fluorescent immunostaining shows CX3CR1^{GFP} IGMs localized within the agrin-expressing ganglionic border (Figure 1C, arrowheads). MyMs are situated outside the ganglia (Figure 1C, arrows), but with their cell bodies adjacent to the agrin+ ganglionic border. Surrounding the ganglia is the periganglionic space (PGS) (Figure 1E, asterisks), which comprises the connective

^aAuthors share co-first authorship.

Abbreviations used in this paper: BBB, blood-brain barrier; BMB, blood-myenteric barrier; CNS, central nervous system; DSS, dextran sulfate sodium; ECM, extracellular matrix; ENS, enteric nervous system; FITC, fluorescein isothiocyanate; GFP, green fluorescent protein; GI, gastrointestinal; Iba1, ionized calcium-binding adapter molecule 1; IBD, inflammatory bowel disease; IGM, intraganglionic macrophage; IL, interleukin; iNOS, inducible nitric oxide synthase; LPS, lipopolysaccharide; MCP-1, monocyte chemoattractant protein-1; MM, muscularis macrophage; MMP, matrix metalloproteinase; MyMs, myenteric plexus macrophages; PAMP, pathogen-associated molecular pattern; PBS, phosphate-buffered saline; PGS, periganglionic space; qPCR, quantitative polymerase chain reaction; STED, stimulated emission depletion; TNF, tumor necrosis factor.



Most current article

© 2021 The Authors. Published by Elsevier Inc. on behalf of the AGA Institute. This is an open access article under the CC BY-NC-ND license (<http://creativecommons.org/licenses/by-nc-nd/4.0/>).

2352-345X

<https://doi.org/10.1016/j.jcmgh.2021.07.003>

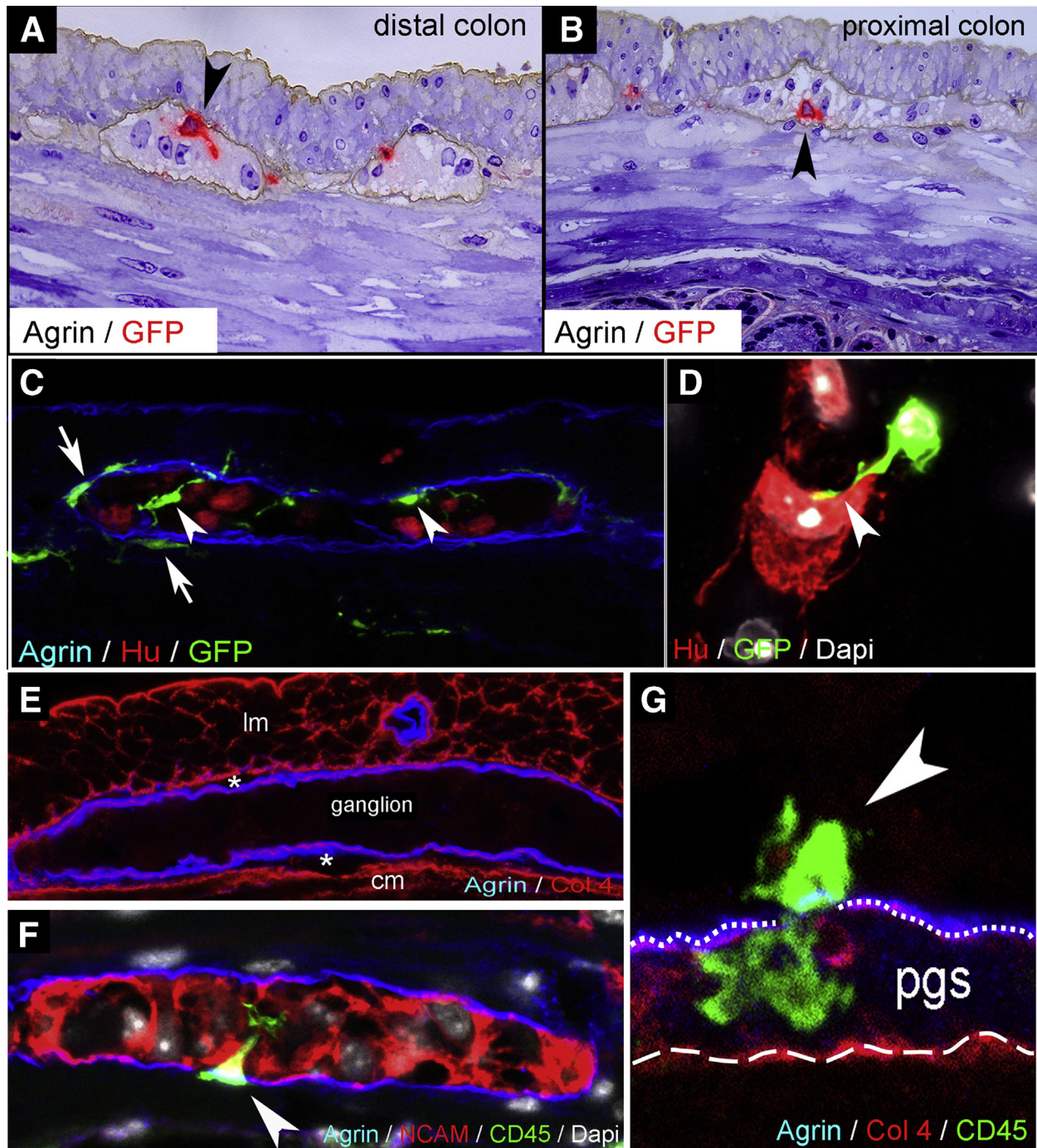


Figure 1. IGMs and their characterization in $CX3CR1^{GFP}$ mouse colon. Double immunolabeling of semithin sections with agrin and GFP was performed on distal (A) and proximal (B) colon sections of adult $CX3CR1^{GFP}$ mice. GFP+ IGMs (red) are present inside the agrin+ basement membrane of the enteric ganglia (brown). Immunofluorescent staining with agrin (ganglionic basement membrane), Hu (enteric neurons), and GFP (macrophages) shows spatially distinct populations of MMs, with IGMs labeled with arrowheads and MyMs in the PGS with arrows (C). GFP+ IGM in physical contact with an enteric neuron (D, arrowhead). Agrin and Col4 immunolabeling shows the ECM capsule surrounding the enteric ganglia (E). The periganglionic space (E, asterisks) is present between the Col4-expressing smooth muscle basement membrane and the Col4+/agrin+ expressing ganglionic basement membrane. Super-resolution imaging of IGMs and the PGS shows a MyM penetrating the ganglionic basement membrane (G, dotted line) and entering the enteric ganglion (F and G, arrowheads). The smooth muscle basement membrane again shows expression of Col4, but not agrin (G, dashed line). cm, circular muscle layer; Im, longitudinal muscle layer.

tissue space between the agrin and collagen type 4 (Col4) expressing ganglionic basement membrane (Figure 1G, dotted line) and the smooth muscle basement membrane expressing Col4 but not agrin (Figure 1G, dashed line). Super-resolution imaging using stimulation emission depletion (STED) microscopy revealed that CD45+CX3CR1+ macrophages are also present in the PGS and can penetrate the ganglionic basement membrane and enter the enteric ganglia (Figure 1F and G, arrowheads). The morphologic features of these cells suggest active migration from the PGS into the intraganglionic space. STED imaging also demonstrates CX3CR1+ macrophages in direct physical contact with Hu-expressing enteric neurons (Figure 1D, arrowhead).

To characterize the immunophenotype of IGMs, we performed confocal microscopy on serial sections of CX3CR1^{GFP} mouse distal colon. Previously it was shown that CX3CR1+ MMs are CD45+, CD11b+, and F4/80+.⁹ Double immunostaining with anti-GFP antibody (Figure 2A) and the macrophage marker CD11b (Figure 2A') confirms coexpression on all MMs including IGMs (Figure 2A", arrowhead). GFP+ IGMs also express colony-stimulating factor 1 receptor (Figure 2B-B"), pan-macrophage marker F4/80 (Figure 2C-C"), and ionized calcium-binding adapter molecule 1 (Iba1) (Figure 2D-D"), which is known to be expressed

by intestinal MMs.²⁹ We find the IGMs present inside the enteric ganglia, which are delineated by agrin expression (Figure 2A" and D") and among Hu+ (Figure 2B") and NCAM+ (Figure 2C") enteric neurons. F4/80 and Iba1 are coexpressed on MMs and IGMs (Figure 2E, circled area; Figure 2F-F", arrowheads). However, Iba1 is not expressed by most submucosal macrophages (Figure 2F-F", arrows). In contrast, macrophages in mucosal lymphatic aggregates express Iba1 and not F4/80 (Figure 2E, dashed line; Figure 2F-F"). These findings suggest that the various subpopulations of intestinal macrophages possess different immunophenotypes, with IGMs expressing CD45, CX3CR1, CD11b, Iba1, F4/80, and colony-stimulating factor 1 receptor.

We compared the total number of MMs in the muscularis propria of CX3CR1^{GFP} mouse colon and found no significant difference between distal and proximal colon (76.03 ± 32.64 vs 73.82 ± 29.26 cell/mm², $P = .4506$). The ratio of IGMs to total MMs is higher in the distal colon, although this difference did not reach statistical significance ($3.26 \% \pm 1.3 \%$ vs $2.12 \% \pm 1.1 \%$, $P = .0977$; Figure 2G). When the density of IGMs is adjusted to ganglionic area, there is a significantly higher density of IGMs in the distal compared with proximal colon (82.37 ± 32.98 vs 50.25 ± 19.6 cell/mm², $P = .0309$; Figure 2H).

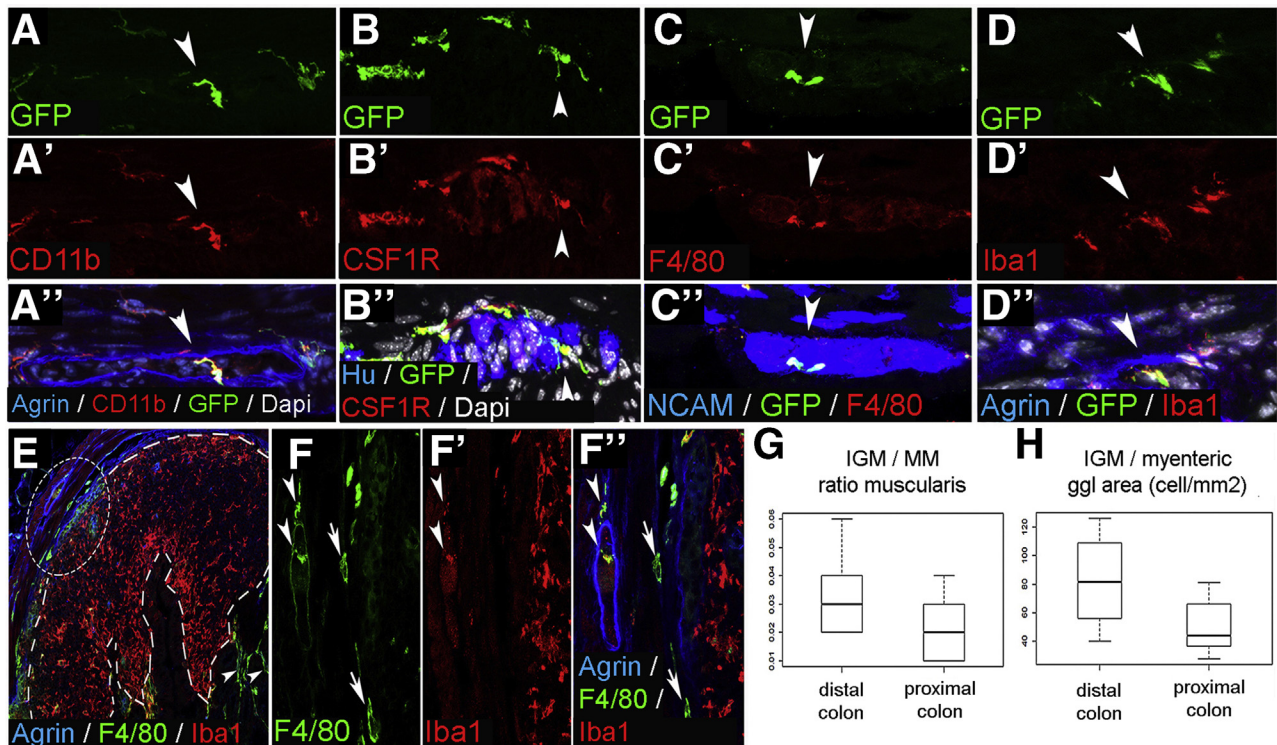


Figure 2. Immunophenotype and spatial distribution of IGMs in CX3CR1^{GFP} mouse colon. GFP+ IGMs are present within the agrin-bordered enteric ganglia and co-express CD11b (A-A"), CSF1R (B-B"), F4/80 (C-C"), and Iba1 (D-D"). F4/80 and Iba1 are co-expressed by MMs and IGMs (F-F", arrowheads, magnified from circled area in E), but Iba1 is not present in submucosal macrophages (F-F", arrows). In lymphatic aggregates of the colonic mucosa (E, area within dashed line), macrophages express Iba1 but not F4/80. Comparison of MM and IGM cell number in the proximal and distal colon of CX3CR1^{GFP} mice shows no significant difference in ratio of IGMs to total MMs (G; $3.26 \% \pm 1.3 \%$ vs $2.12 \% \pm 1.1 \%$, $P = .0977$, $n = 8$). However, the number of IGMs is significantly higher in distal colon compared with proximal colon when adjusted to myenteric ganglion area (H; 82.37 ± 32.98 vs 50.25 ± 19.6 cell/mm², $P = .0309$, $n = 8$).

IGMs Are Structurally Distinct From Extraganglionic Macrophages

To study IGM ultrastructure and their microenvironment, electron microscopy was performed on the distal colon of mice. In the ganglia, enteric neurons (Figure 3A, dashed line) are characterized by a condensed cytoplasm, euchromatic nucleus, and prominent nucleoli. In contrast, enteric glial cells exhibit a euchromatic nucleus, anchored heterochromatin, and a cytoplasm of lower density (Figure 3A).^{12,13} Enteric ganglia also contain electron-dense, highly vacuolated cells that display a distinct morphology from neural and glial cells. These are the IGMs (Figure 3A). Formation of pseudopodia around

glial cell processes (Figure 3A–A', arrows) suggests a phagocytic function of the IGM. Despite signs of cellular degeneration, including swollen mitochondria (Figure 3A') and massive cytoplasmic vacuolization, the nucleus of the IGM shows no sign of apoptosis (Figure 3A, asterisk). Figure 3B shows the morphologic difference between periganglionic macrophages and IGMs. The IGM is characterized by a low nucleus/cytoplasm ratio and a segmented non-apoptotic nucleus. IGMs also exhibit an extensive Golgi and vesicular apparatus (Figure 3B, dashed circle) and active formation of phagocytic vesicles (Figure 3B, asterisk). Some IGMs display mostly empty vacuoles (Figure 3C, dotted rectangle; Figure 3D,

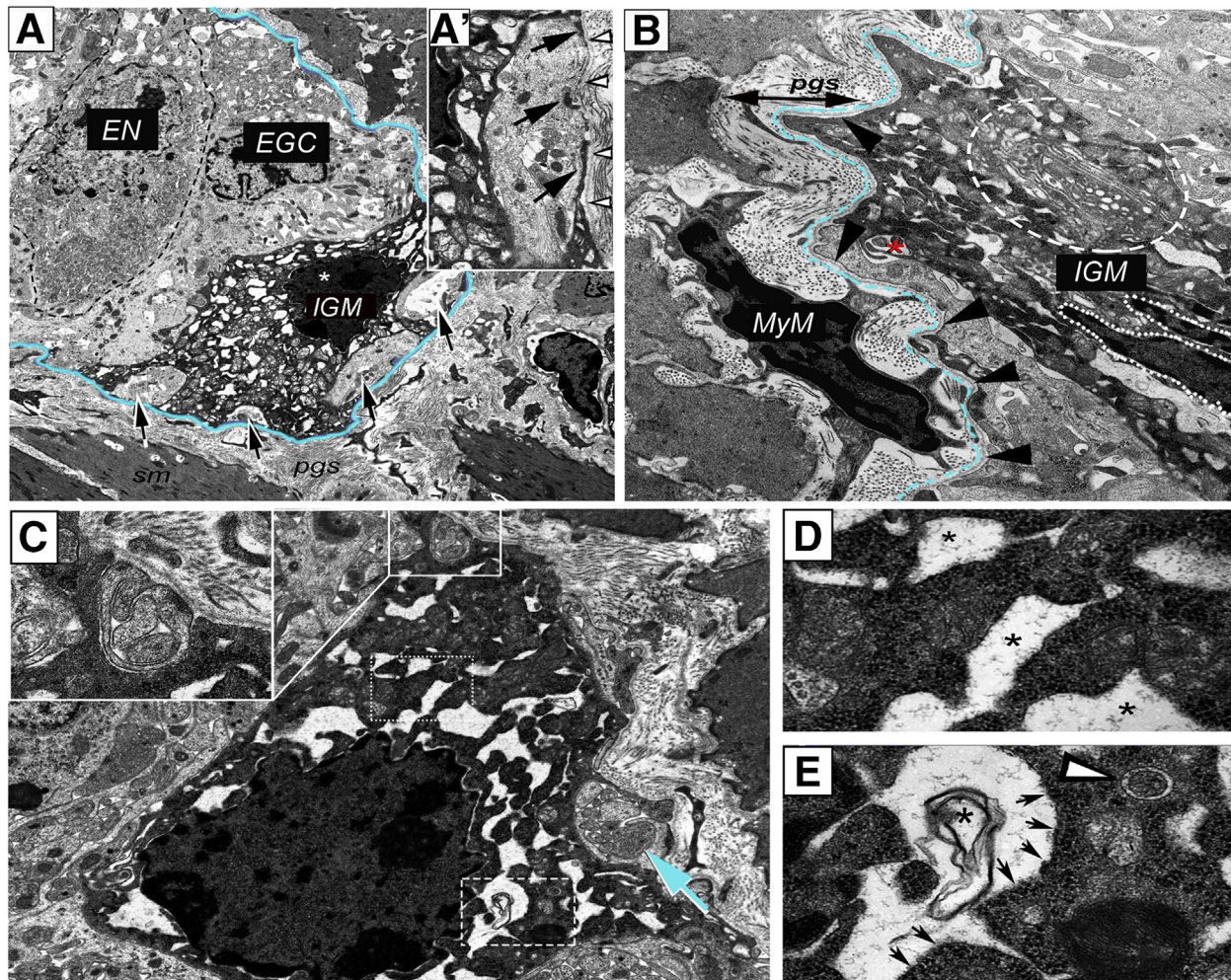


Figure 3. Ultrastructure of IGMs in the mouse colon. Low magnification image of a myenteric ganglion (A) shows electron-dense IGM, displaying distinct morphology from enteric glial cells (EGC) and enteric neurons (EN). *Dashed line* labels EN with condensed cytoplasm. IGM (* marks IGM nucleus) shows active phagocytosis, with multiple pseudopodia around glial cell processes (A–A', arrows). IGM is situated internal to the basement membrane of the enteric ganglion (A, blue line; A', arrowheads). Periganglionic MyM exhibits a high nucleus/cytoplasm ratio, in contrast to IGM, which is characterized by hypertrophic cytoplasm, abundant mitochondria, extensive vacuolization, and well-developed Golgi apparatus (B, encircled area). A phagocytic vesicle is seen (B, asterisk). The ganglionic basement membrane is continuous and uninterrupted on external surface of IGM (B, arrowheads, with basement membrane located under dashed blue line). IGMs exhibit mostly empty vacuoles (C, dotted line; enlarged in D, where vacuoles are marked by asterisks), with lined-up ribosomes on their borders (E, arrows) and occasional membranous whorls are present (C, dashed line; enlarged in E, asterisk). Evidence of phagocytic activity is seen in IGM (C, inset and arrow), but autophagosomes are rarely seen (E, arrowhead). EGC, enteric glial cell; EN, enteric neuron.

asterisks), with lined-up ribosomes on the edge (Figure 3C, dashed rectangle; Figure 3E, arrows) and occasionally filled with membranous whorls (Figure 3E, asterisk). Signs of pseudopodia and phagosome formation are present in the IGM (Figure 3C, inset). Although an occasional autophagosome is seen (Figure 3E, arrowhead), the IGMs show no morphologic signs of significant autophagosome formation.

Enteric Ganglia Are Surrounded by a Barrier Formed By ECM and Glial End-Feet

Immunofluorescence was performed on the distal colon of PLP1^{GFP} mice (Figure 4A–C). Proteolipid protein 1 is expressed by enteric glial cells.³⁰ Confocal imaging reveals that GFP⁺ enteric glia establish an almost continuous layer of glial end-feet (Figure 4A) internal to the agrin-expressing ECM layer (Figure 4A). IGMs are located internal to this glial

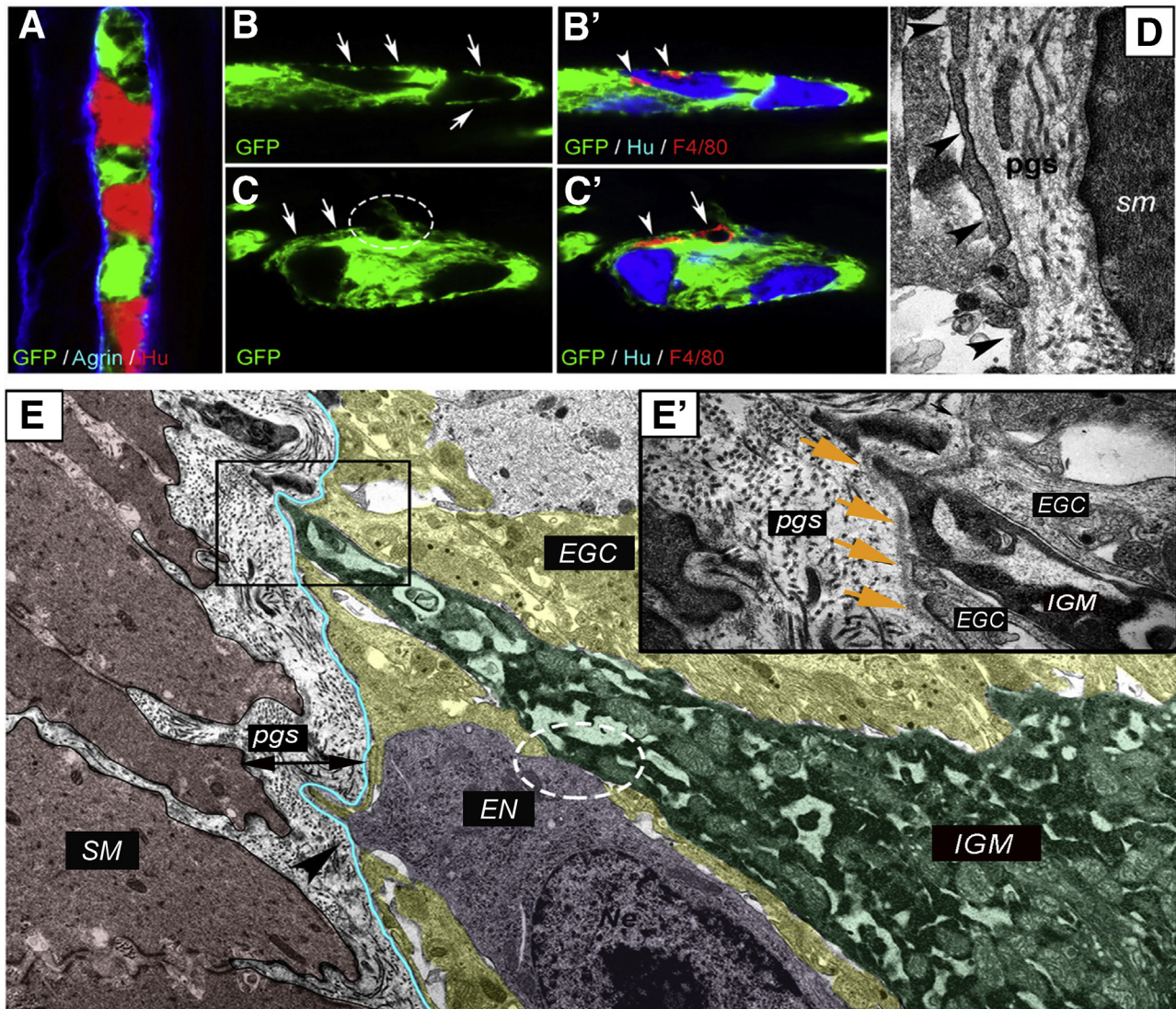


Figure 4. Morphology of glial limiting membrane and enteric ganglion basement membrane in the mouse colon. An enteric ganglion in the distal colon of a PLP1^{GFP} mouse shows GFP-expressing glial cells, agrin-expressing ganglionic basement membrane, and Hu⁺ neurons (A). Glial end-feet establish a continuous layer around the enteric ganglia, occasionally interrupted by small gaps (B, arrows). F4/80⁺ IGMs are located internal to the glial end-feet (B', arrowheads) and among Hu⁺ enteric neurons. Disruption of glial end-feet (C, encircled area) is present at suspected entry points of F4/80⁺ macrophages (C', arrow). Continuity of the glial end-feet is intact around the macrophage process (C', arrowhead) but not around its cell body (C', arrow). Electron micrograph of PGS shows structure of the enteric ganglion barrier, formed by a layer of glial end-feet (D, arrowheads) and the basement membrane. In the microenvironment of an IGM (E, green shaded area), the ganglionic barrier includes glial cells (EGC; yellow shaded area) and ganglionic basement membrane (blue line). High magnification image shows IGM between 2 glial end-feet, delineated from the PGS by a continuous basement membrane (E, squared area is magnified in E', where arrows denote basement membrane). Enteric neuron (E, magenta shaded area) establishes physical contact with IGM (E, circled area) and disrupts the continuous glial end-feet layer at suspected fiber exit point (E, arrowhead). EGC, enteric glial cell; EN, enteric neuron; SM, smooth muscle.

barrier (Figure 4B', arrowheads), intermingling with Hu+ enteric neurons. At sites where glial end-feet disruption occurs (Figure 4C, circle), an F4/80+ macrophage is seen (Figure 4C', arrow). Interestingly, the continuity of glial end-feet is present around the process of the same macrophage (Figure 4C, arrows; C', arrowhead) but not around its cell body (Figure 4C, circle; C', arrow). Figure 4D shows the ultrastructure of the glial end-feet (arrowheads), with the continuous ganglionic basement membrane and the PGS surrounding it. IGMs in the ganglionic microenvironment are adjacent to enteric glial cells and enteric neurons (Figure 4E). Although glial end-feet closely bound the IGMs inside the ganglion, they do not entirely separate them from the PGS (Figure 4E'). As can be seen, the continuity of the glial end-feet layer is interrupted by IGMs (Figure 4E, boxed area) and also by enteric neurons, most likely at sites where neural fibers exit the ganglion (Figure 4E, arrowhead).

FITC-dextran assays were performed to assess the barrier function of the ECM and glial end-feet around the enteric ganglia, because this is reminiscent of the BBB. FITC-dextran 4kDa was injected into the tail vein of wild-type C57BL/6 mice. Animals were killed after 10 minutes, and the distal colon, liver, and cerebellum were removed (Figure 5A). At 10 minutes after FITC administration, fluorescent particles are scattered in the submucosa and mucosa of the gut (Figure 5B) and around blood vessels (Figure 5B, arrow), whereas the muscularis shows no green fluorescence (Figure 5B, dashed lines). At this time point, only a few F4/80+ cells co-localize with FITC (Figure 5C, arrowheads), whereas most macrophages do not contain fluorescent particles (Figure 5C, arrows). In the liver where capillaries are discontinuous, having 30- to 40- μ m diameter openings in their endothelium, diffuse green fluorescent signal is already present at 10 minutes (Figure 6A), with only scattered expression in the colonic mucosa of the same animal (Figure 6B). FITC signal was not detected in the cerebellar interstitium of experimental mice (Figure 6C). At 45 minutes after FITC injection, signal is present in all layers of the gut wall but not within the enteric ganglia (Figure 5D-F'). As shown in Figure 5F-F', fluorescence surrounds the agrin-expressing borders of the enteric ganglia and diffusely stains the PGS, but no fluorescence is detected in the intraganglionic space. After 60 minutes, intestinal F4/80+ macrophages contain phagocytosed FITC+ particles (Figure 5G, arrowheads). Diffuse FITC signal in the PGS persists, and MyMs incorporate fluorescent particles as well (Figure 5H-H', arrowheads). Interestingly, at 60 minutes, F4/80+ IGMs also contain FITC (Figure 5I-I', arrowheads). Because FITC molecules normally cannot penetrate the ganglionic barrier (Figure 5I, arrows), the presence of FITC in the ganglion suggests that IGMs, capable of phagocytosis, enter the ganglia from the PGS. At 60 minutes after FITC injection, all F4/80+ Kupffer cells in the liver are filled with fluorescent label (Figure 6D), and high levels of macrophage-FITC colocalization are also present in the colon (Figure 6E-E'). These findings are strongly suggestive of the presence of a BMB.

DSS-Induced Colitis Induces Degradation of the Periganglionic ECM via a M1-Macrophage-Dependent Process

DSS induces experimental colitis by disrupting the intestinal epithelial barrier.²⁷ Treatment with liposome-encapsulated clodronate (L-clodronate) produces temporary depletion of tissue and blood mononuclear phagocytes.²⁸ Thus, induction of DSS colitis followed by treatment with L-clodronate blocks macrophage recruitment by depleting the monocyte pool in the blood and bone marrow, thereby allowing us to study colitis in the absence of macrophages (Figure 7A). Figure 7B and D show the typical colonic shortening associated with colitis and its reversal in mice treated with clodronate. General inflammatory signs, such as muscularis thickening (Figure 7C), and disease activity index (Figure 7E) all show significant improvement in animals receiving L-clodronate treatment. Figure 7F shows the histology of the colon after DSS treatment and with concurrent DSS-clodronate administration. Whereas the ECM barrier surrounding the enteric ganglia normally contains a continuous layer of agrin and Col4 (Fig. 7G-G'), DSS-induced acute colitis is associated with degradation of this ECM barrier and extensive infiltration of F4/80+ macrophages (Figure 7H-H' and J), including IGM infiltration into the Hu+ enteric ganglia (Figure 7H, inset). Interestingly, the agrin expression in the vascular basement membrane of muscularis vessels remains intact (Figure 7H', arrowhead). In the inflammatory infiltrate 2 types of F4/80+ cells are distinguishable according to cellular morphology³¹: ramified, bipolar, or stellate-shaped MMs (Figure 7H', inset) and round monocytes with kidney-shaped nuclei (Fig 7H', inset). L-clodronate treatment, which depletes macrophages from the muscularis propria, leads to preservation of normal ECM patterning, with intact agrin and Col4 expression in the BMB (Figure 7I-I' and J). The increased density of F4/80+ MMs (Figure 7K) and IGMs (Figure 7L and M) observed after DSS treatment is not seen with L-clodronate treatment. No significant difference was found in the relative distribution of MMs in different layers of the gut wall (Figure 7N).

Neutrophil Infiltration Is Not Required for Colitis-Induced Degradation of the Enteric Ganglia

To understand to what extent neutrophils contribute to inflammation in the muscularis propria during DSS-colitis, we performed quantitative polymerase chain reaction (qPCR) and immunofluorescence with the neutrophil markers Ly6G and MPO. Ly6G RNA expression was increased in whole gut and isolated muscularis after DSS, but not after concurrent L-clodronate treatment (Figure 8A and B). The mucosa and submucosa both exhibit massive infiltration of Ly6G-expressing neutrophils, comparable to the number of Iba1+ macrophages (Figure 8I). In contrast, the muscularis only has a modest infiltration of Ly6G+ cells compared with MMs (Figure 8I', R, and S). Note that Iba1 is used as a marker for F4/80+ macrophages because their cellular expression in the muscularis overlaps completely (Figure 9A-C). No Ly6G+ neutrophils are detected adjacent to or within enteric ganglia (Figure 8I', inset). Very few

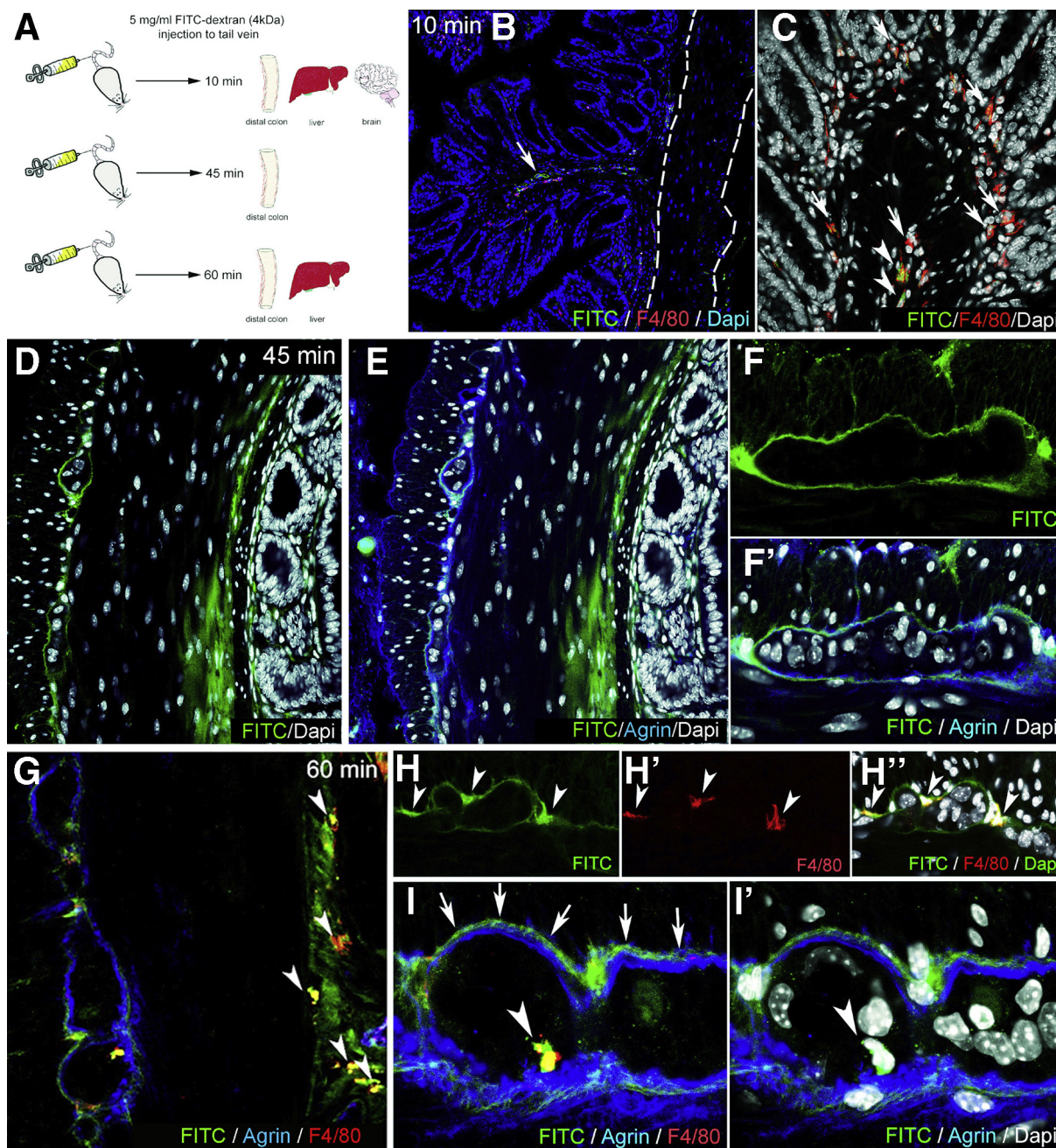


Figure 5. Enteric ganglia are surrounded by a protective myenteric plexus barrier. Schematic drawing shows experimental design of FITC-dextran assays, where wild-type C57BL/6 mice receive intravenous FITC-dextran (50 mg/mL) and are killed 10, 45, and 60 minutes later (A). At 10 minutes after FITC-dextran loading, scattered green fluorescence is present in the lamina propria (B, arrow) but not the muscularis propria (B, dashed line). Most F4/80⁺ macrophages in the colon do not contain FITC particles (C, arrows), but some do (C, arrowheads). At 45 minutes after injection, diffuse FITC signal appears in the mucosa and submucosa (D and E). Strong FITC signal is also present around the enteric ganglia but not within them (F–F'). At 60 minutes, F4/80⁺ macrophages contain FITC (G, arrowheads). MyMs expressing FITC are seen in the PGS (H–H', arrowheads; I, arrows), and FITC-loaded IGMs have entered into the intraganglionic compartment (I–I', arrowhead).

Ly6G⁺ cells are detected in the muscularis propria of the colon of control animals (Figure 8R and S), and only a low number are present in DSS+L-clodronate treated mice (Figure 8R and S), mostly neutrophils in the mucosa (Figure 8O). Double staining with anti-myeloperoxidase antibody shows that the majority of Ly6G⁺ neutrophils

coexpress myeloperoxidase in all layers of the inflamed gut (Figure 9D–F'). In summary, neutrophil infiltration is high in the mucosal and submucosal layers of the gut during DSS colitis but less so in the muscularis propria, where Ly6G⁺ cells do not appear to interact physically with the enteric ganglia as the macrophages do.

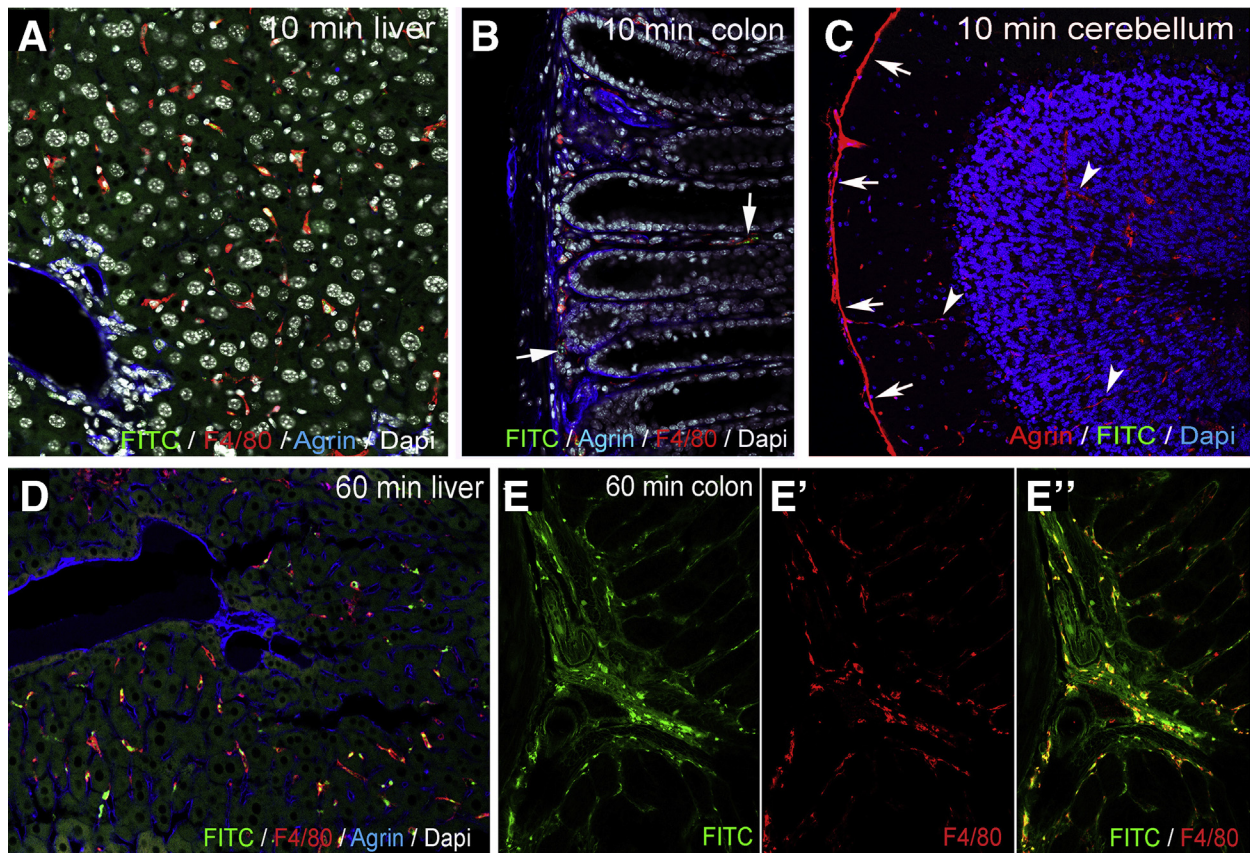


Figure 6. FITC-dextran assays: control organs. At 10 minutes after FITC injection, diffuse fluorescence is present in the liver (A), but only scattered FITC particles are visible in the colon of the same animal (B), and no FITC is seen in the cerebellum (C). Agrin is expressed around blood vessels (C, arrowheads) and in the external glial limiting membrane (C, arrows). At 60 minutes after FITC administration, most Kupffer cells incorporate FITC in the liver (D). In the colon, diffuse interstitial FITC signal is present in the mucosa and submucosa (E) and in most F4/80+ macrophages (E'–E'').

Dynamic Changes in Macrophage Polarization Occur in the Muscularis in the Setting of Colitis

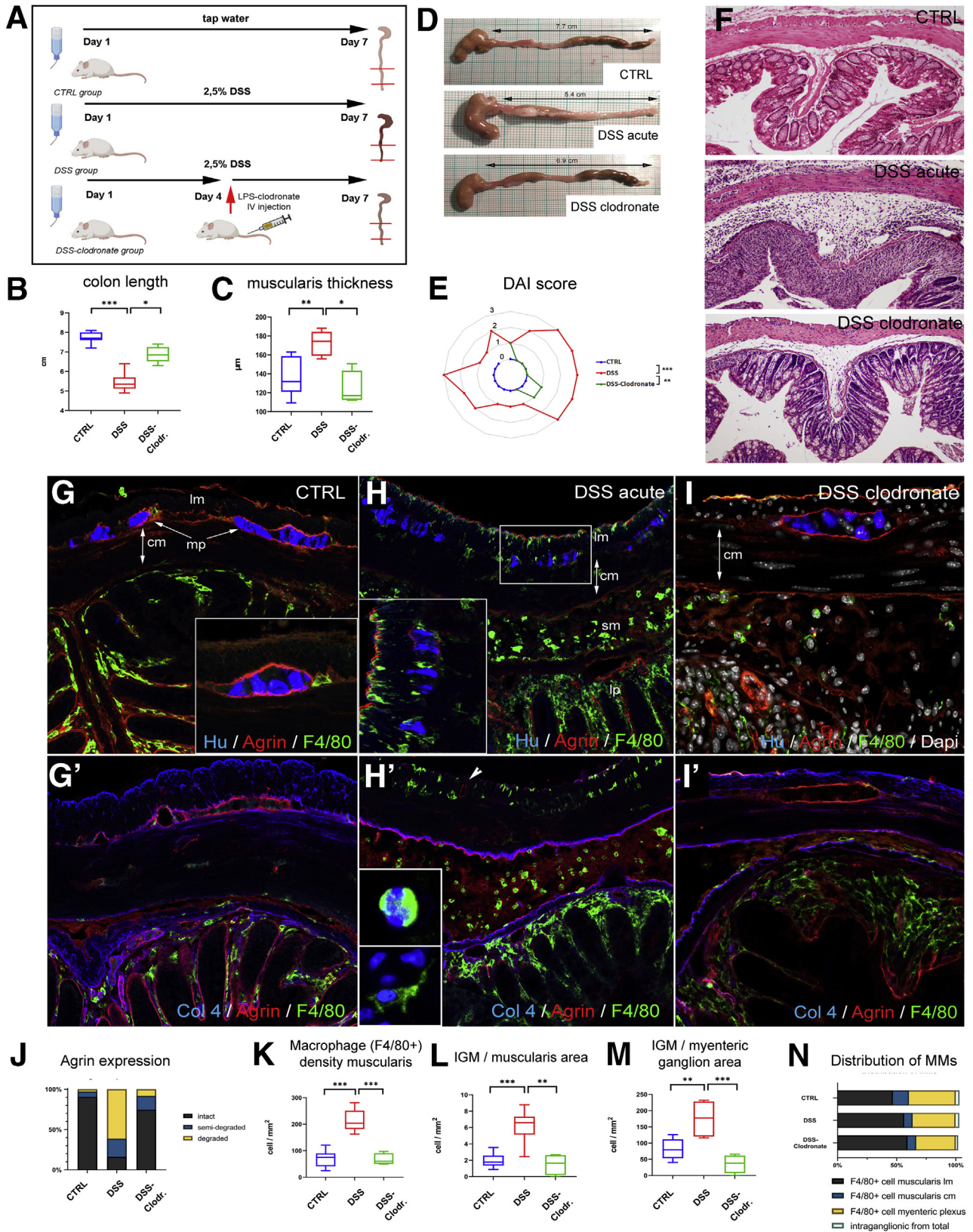
Colitis was previously shown to be associated with a shift to M1-macrophage polarization^{32,33} and increased expression of inflammatory mediators.^{34,35} Expression of inducible nitric oxide synthase (iNOS) (a marker of M1-polarization³⁶) significantly increases in whole colon and isolated muscularis of DSS-treated mice and reverts to baseline in DSS+L-clodronate treated animals (Figure 8C and D). Interestingly, RNA expression of M2-polarization markers CD163 and ARG1³⁶ show no significant change during the course of DSS treatment or concurrent L-clodronate injection (Figure 8E–H). Immunofluorescence for iNOS in DSS-treated mice reveals expression in clusters of F4/80+ macrophages and monocytes in the mucosa (Figure 8J), submucosa (Figure 8J'), and serosa (Figure 8J''). A few F4/80-negative cells also express iNOS (Figure 8J, asterisks). After DSS, iNOS is expressed in 31 % (Figure 8Q) of F4/80+ MMs (Figure 8K–K', arrowheads) and monocytes (Figure 8K'', arrowheads), whereas 69 % of F4/80+ cells do not express iNOS (Figure 8K', arrow, and Q'). Interestingly, multiple CD45-negative non-hematopoietic cells express iNOS in the inflamed colon (Figure 8M, arrows), instead expressing smooth muscle actin (Figure 8M).

Area-adjusted cell counting reveals that 59 % of iNOS+ cells in the muscularis after DSS treatment are SMA+ smooth muscle cells (Figure 8Q). If DSS treatment is interrupted by L-clodronate administration, the number of iNOS+ cells significantly decreases in the muscularis (Figure 8R and S), leaving 96 % of F4/80+ cells iNOS- (Figure 8Q'), and of the remaining iNOS+ cells, 93 % are smooth muscle cells (Figure 8P and Q). Quantitative data on cell counting are shown in Supplementary Material. Our findings reveal that iNOS expression significantly increases in the colonic muscularis, where, in addition to macrophages, smooth muscle cells also express the molecule. Furthermore, L-clodronate treatment reverses the shift toward M1-polarization in the muscularis propria but does not affect M2-associated molecular markers such as ARG-1 and CD163.

Along with M1 macrophage polarization, the RNA expression of proinflammatory cytokines interleukin (IL) 1A, IL1B, tumor necrosis factor (TNF) alpha, and monocyte chemoattractant protein-1 (MCP-1) all show significant increases as a consequence of DSS treatment (Figure 10A, C, G, and I). Interestingly, the inflammation is not limited to the mucosa, because isolated muscularis tissue exhibits similarly elevated RNA expression for these markers (Figure 10B, D, H, and J). IL10 has been shown to be

expressed in the gut mucosa at later stages of colitis to initiate fibrosis and regeneration in severely inflamed tissues.³⁵ Here IL10 RNA levels increase more than 10-fold in

whole gut (Figure 10E) and slightly in the muscularis (Figure 10F). Concurrent L-clodronate treatment decreases the expression of IL1A, IL1B, and IL10 significantly in whole



gut of experimental mice (Figure 10A, C, and E). In the muscularis, the reversal effect of L-clodronate is statistically significant for TNF and MCP-1 expression (Figure 10H and J) but not for IL1A and IL1B expression (Figure 10B and D). IL10 expression in the muscularis is not affected by L-clodronate treatment (Figure 10F).

Double immunofluorescence was performed to reveal the cell populations that express TNF, a master regulator of the inflammatory response. After induction of DSS colitis, TNF protein is expressed by the mucosal epithelial lining³⁷ (Figure 10K, dashed line), serosal F4/80+ cells (Figure 10K, arrowheads; and Figure 10L, asterisks), clusters of mucosal macrophages (Figure 10M), and enteric ganglia (Figure 10K and N, dashed line). Interestingly, F4/80+ MyMs (Figure 10K and N, arrows) and IGMs (Figure 10N, asterisk) show no co-localization with TNF expression. In DSS+L-clodronate treated mice enteric ganglia do not express TNF (Figure 10O, arrows), whereas clusters of mucosal epithelial cells (Figure 10P, inset, dashed line) and F4/80+ macrophages (Figure 10P, arrows) show persistent TNF production despite L-clodronate treatment. In the absence of MMs, TNF production decreases in the muscularis, and the major source of TNF is not the macrophages, but rather the enteric ganglia. This finding implies an indirect crosstalk between these cell populations that is consistent with other studies in different contexts.^{2,18}

Matrix Metalloproteinase 10 Shows Strong Expression in the Muscularis and Myenteric Plexus After DSS Treatment, Reversed by the Depletion of MMs

According to RNA sequencing analysis earlier reported (accession number : PRJNA687627) in DSS-treated vs control mice, matrix metalloproteases (MMPs) are increased in colitis (Figure 11A, Table 1).³⁸ Collagen 4 is the substrate of

gelatinase MMP2, whereas agrin is the substrate of stromelysin MMP10. According to qPCR, both MMPs exhibit increased RNA expression in the gut wall after DSS and return to baseline with L-clodronate injection (Figure 11B and D). In the muscularis specifically, MMP2 expression does not change significantly (Figure 11C), whereas MMP10 expression increases nearly 2-fold after DSS (Figure 11E).

DSS induces patchy expression of MMP10 protein in the mucosa and submucosa, co-localizing with agrin expression (Figure 11F, encircled areas) and with F4/80+ cells (Figure 11F, inset, arrowheads). In the muscularis, MMP10 is expressed diffusely in the longitudinal muscle layer and inside enteric ganglia (Figure 11F, arrows and G, dashed line). Apart from enteric neurons (Figure 11H), F4/80+ monocytes (Figure 11G, arrowhead and I) and MMs (Figure 11J) also express MMP10. In contrast with DSS-treated animals, control (Figure 11K) and DSS+L-clodronate treated mice (Figure 11L) exhibit virtually no expression of MMP10 in the muscularis layer or in the enteric ganglia (Figure 11L, arrows), whereas scattered F4/80-negative cells (Figure 11K, arrowheads) and F4/80+ monocytes (Figure 11L, arrowheads) express MMP10 in the mucosa of control and L-clodronate treated animals, respectively.

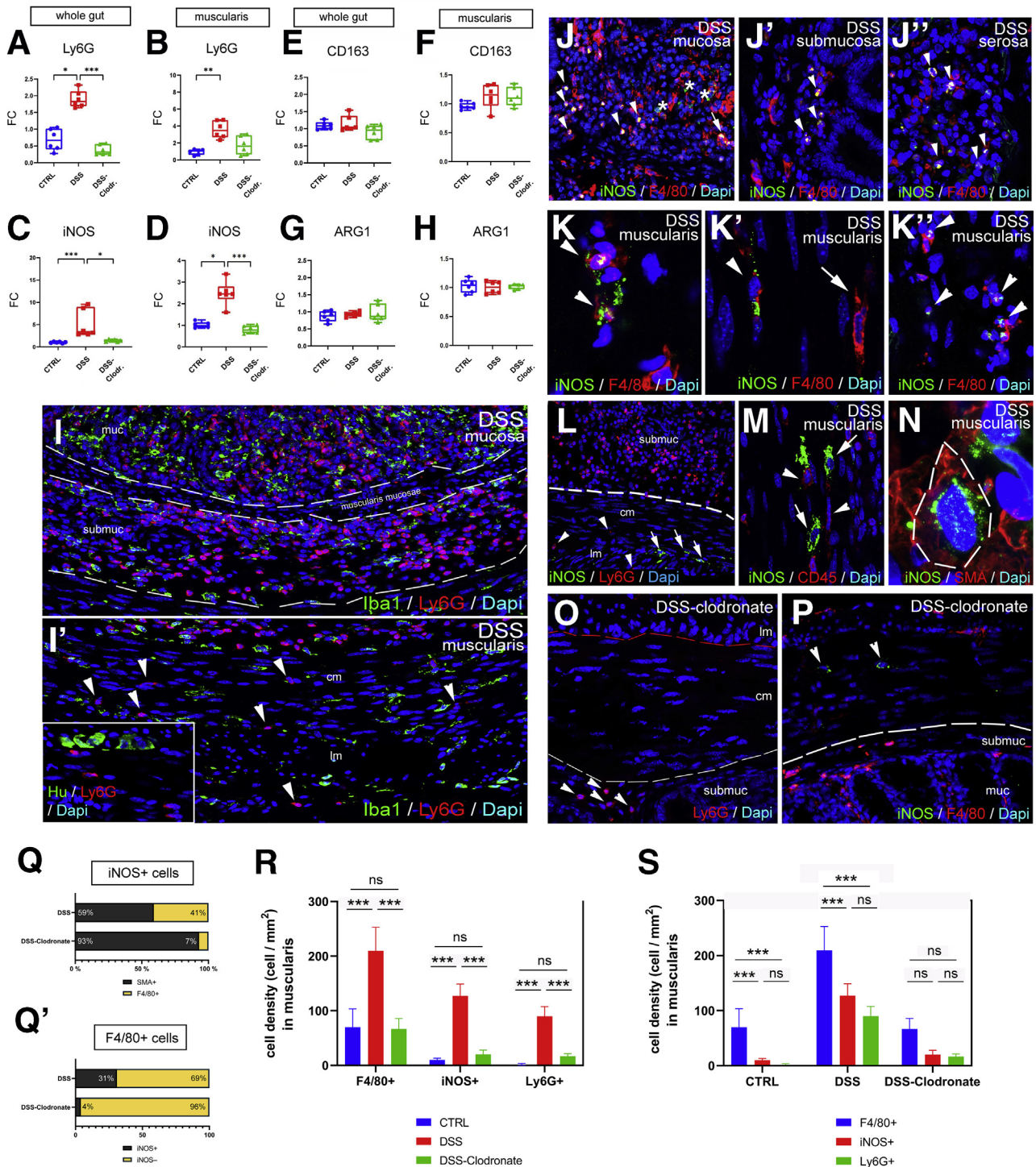
DSS-Induced Colitis Disrupts the Ganglionic Basement Membrane Causing BMB Dysfunction

Electron microscopy of enteric ganglia in DSS-treated mice (Figure 12) reveals the disruption (Figure 12, boxed area, Figure 12A', arrows) or absence (Figure 12A'', arrows) of the ganglionic basement membrane and the accumulation of collagen fibers in the PGS (Figure 12A'). To test the functional integrity of the BMB barrier in colitis, we injected DSS- and DSS+L-clodronate treated mice on day 7 with FITC dextran as described above and

Figure 7. (See previous page). DSS treatment leads to colitis and disruption of periganglionic ECM via a macrophage-dependent mechanism. Schematic drawing shows experimental design of DSS treatment and concurrent L-clodronate administration (A). Colonic shortening characteristic of DSS-induced colitis was observed, but not in mice receiving clodronate treatment (B and D). Muscularis propria was thickened in DSS-treated mice compared with controls (172 ± 11.6 vs $136.8 \pm 18.8 \mu\text{m}$, $P = .003$; C) and with clodronate treated mice (F; 172 ± 11.6 vs $124.2 \pm 15.7 \mu\text{m}$, $P = .022$; C). Radar chart shows higher disease activity index (DAI) scores in DSS versus controls (2 ± 0.8 vs 0 , $P < .001$) and clodronate treated animals (2 ± 0.8 vs 0.4 ± 0.5 , $P = .003$; E). L-clodronate treatment ameliorates DSS-induced colitis based on histopathologic assessment with H&E staining (F). Agrin (G) and Col4 (G') are normally expressed around the enteric ganglia but are severely disrupted after 7 days of DSS treatment (H and H'). DSS colitis is associated with extensive F4/80+ macrophage infiltration in the distal colon, including within the ganglia (H, inset; H', arrowhead). In animals treated with liposomal clodronate during DSS administration, macrophages are absent from the muscularis propria (I-I'). Although inflammatory signs are still present in the mucosa and lamina propria, normal ECM patterning is preserved, with intact agrin and Col4 around the ganglia (I-I'). DSS leads to agrin degradation in the BMB, where 61 % and 22 % of enteric ganglia exhibit a degraded or semi-degraded agrin layer, respectively, and only 16 % remain intact. In clodronate treated mice, only 17 % and 8 % of enteric ganglia have a degraded or semi-degraded periganglionic agrin layer, respectively, with 75 % intact (J). F4/80+ MM density was significantly increased in DSS-treated mice compared with controls (213.9 ± 39 vs $70.4 \pm 28.9 \text{ cell/mm}^2$, $P < .001$; K) and clodronate treated mice (213.9 ± 39 vs $66.9 \pm 19 \text{ cell/mm}^2$, $P < .001$; K). Cellular density of IGMs adjusted to muscularis area was increased after DSS-colitis compared with controls (6.3 ± 1.8 vs $1.9 \pm 0.8 \text{ cell/mm}^2$, $P < .001$; L) and clodronate treated animals (H; 6.3 ± 1.8 vs $1.5 \pm 1.1 \text{ cell/mm}^2$, $P = .002$; L). DSS treatment also increased IGM density in DSS-treated compared with control mice (174.9 ± 47.7 vs $81.5 \pm 28.7 \text{ cell/mm}^2$, $P = .003$) and with clodronate treated mice (174.9 ± 47.7 vs $35.7 \pm 24.4 \text{ cell/mm}^2$, $P < .001$) when adjusted to total myenteric ganglion area (M). Relative distribution of MMs in different anatomic layers did not differ among groups (N). cm, circular muscle; DAI, disease activity index; lm, longitudinal muscle; lp, lamina propria; mp, myenteric plexus; sm, submucosa.

removed the distal colon after 15, 45, and 60 minutes. After 60 minutes, FITC particles penetrate the disrupted BMB, with increased intraganglionic fluorescence in DSS-treated animals (Figure 12B-B') as compared with untreated controls (Figure 5I-I'). In contrast, animals receiving both DSS and L-clodronate show accumulation of FITC only around the enteric ganglia but not within them

(Figure 12C-C'). Figure 12D-F shows the mean fluorescent intensity curve measured in whole gut cross sections, muscularis, and intraganglionic areas after 10, 45, and 60 minutes of FITC injection. Note the significant increase in intraganglionic fluorescence after DSS treatment as compared with control and DSS+L-clodronate treatment (Figure 12F).



DSS Colitis Is Associated With Enteric Neuroinflammation, Including Neural Hypertrophy, Glial Swelling, and Submucosal Plexus Degeneration

In addition to infiltration of the muscularis by a variety of immune cells, DSS colitis also causes significant morphologic changes inside the myenteric plexus. Enteric glial cells, which create the glial limiting membrane, rearrange from a parallel (Figure 4D, arrowheads) to perpendicular orientation (Figure 13A, yellow shaded area) relative to the ganglionic basement membrane (Figure 13A, blue dashed line). Moreover, after DSS, glia exhibit a swollen morphology compared with control (Figure 13B and C). Enteric neurons (Figure 13D, magenta shaded area) acquire multiple lipid droplets (Figure 13D, arrows and F, asterisks), many mitochondria (Figure 13E, asterisks), and increased rough endoplasmic reticulum (Figure 13F, arrow). Morphometry identifies a significant increase in myenteric ganglion density (Figure 13H), without a concomitant increase in neural cell density (Figure 13G) or neurons per ganglion (Figure 13I). The colitis-associated hyperganglionosis is reversed by concurrent L-clodronate treatment (Figure 13H). Interestingly, DSS treatment causes a sharp decline in the number of submucosal neurons, and this returns to baseline with L-clodronate treatment (Figure 13J).

Discussion

We describe the existence of a physical BMB at an ultrastructural level that is composed of ECM proteins (agrin and Col4) and enteric glial end-feet reminiscent of the BBB. MyMs were observed to actively transmigrate through the BMB and transform into morphologically distinct IGMs, suggesting these cells are capable of BMB remodeling. The BMB was demonstrated to possess a functional role, as shown by its ability to restrict the entry of 4 kDa dextran

into the myenteric plexus. During conditions of inflammation, the integrity of the BMB was compromised via degradation of its ECM constituents in a macrophage-dependent manner. These data for the first time demonstrate that the myenteric plexus can be directly exposed to extra-ganglionic factors during inflammation and offer a mechanism for enteric neuroinflammation and dysfunction in chronic inflammatory GI disorders.

The BBB serves to restrict the passage of cells, proteins, pathogens, and PAMPs between the blood and CNS microenvironment to protect the brain from inflammation and injury. We find that the structures of the BMB are reminiscent of those of the BBB. The BBB is composed of a continuous layer of glial end-feet³⁹ called the limiting glial membrane,⁴⁰ ECM proteins, and a basement membrane between the processes of astrocytes and the non-fenestrated endothelial cells.⁴¹ Similarly, enteric ganglia are separated from the surrounding interstitial tissues of the gut wall by layers of cellular and ECM components. End-feet of PLP1+ enteric glial cells organize into a cellular layer surrounded externally by a ganglionic basement membrane that expresses agrin and Col4. Interestingly, the molecular structure of this barrier resembles the external glial limiting membrane of the BBB, with both possessing strong agrin expression. Of note, in vertebrate development, agrin accumulates on brain capillaries around the time when the vasculature becomes impermeable.^{42,43} Because agrin knockout mice die at birth and ENS-specific deletion of agrin is not available, no study has examined the alterations specific to the ENS-associated ECM in inflammation and injury.

Previous studies have shown that the impenetrable perineurium that surrounds peripheral ganglia is absent in the ENS.²³ The microenvironment of the avascular enteric ganglia and nerve fibers are exposed to extracellular fluid by permeable blood vessels present in adjacent tissues of the gut.²⁴ The permeability of this barrier was tested using

Figure 8. (See previous page). DSS treatment is associated with neutrophil infiltration and increases expression of iNOS in macrophages and smooth muscle cells in a macrophage-dependent fashion. Graphs show relative RNA expression (fold change, FC) of macrophage and neutrophil markers in whole gut and isolated muscularis samples. Quantitative PCR shows significantly higher expression of neutrophil marker Ly6g in DSS-treated vs control (1.82 vs 0.66, $P = .02$; A) and vs DSS+ clodronate treated (1.82 vs 0.31, $P < .001$; A) mice in whole gut and DSS-treated vs control (3.47 vs 1.08, $P < .001$; B) muscularis. M1-macrophage marker iNOS RNA is significantly overexpressed in DSS-treated vs control (4.24 vs 0.87, $P < .001$; C) and vs DSS+ clodronate treated animals (4.24 vs 1.53, $P = .045$; C) in whole gut and in muscularis (2.45 vs 0.97, $P = .02$, and 2.45 vs 0.78, $P < .001$; D), respectively. M2-macrophage markers CD163 and ARG1 showed no significant difference (E–H). Immunofluorescence shows that in DSS-treated animals, Ly6G+ neutrophils are predominant in the mucosa and submucosa (I) but only slightly increased in the muscularis (I', arrowheads), where Iba1+ macrophages dominate. Ly6G expression does not co-localize with Iba1 (I–I'). In the mucosa, submucosa, and serosa, iNOS is expressed in F4/80+ monocytes (J–J', arrowheads) and occasionally in macrophages (J, arrow) and F4/80- cells (J, asterisk). In the muscularis, F4/80+ macrophages (K–K', arrowheads), monocytes (K", arrowheads), and CD45-negative non-hematopoietic cells express the iNOS protein (M, arrows). Multiple CD45+ cells do not express iNOS (M, arrowhead). iNOS (L, arrows) is not expressed in Ly6G+ neutrophils (L, arrowheads) in the muscularis layer. Double labeling with SMA shows smooth muscle expression of iNOS (N, dashed line). With concurrent L-clodronate administration, DSS-treated mice exhibit a low number of Ly6G+ neutrophils restricted to the submucosa (O, arrowheads) and a decreased number of iNOS+ smooth muscle cells in the muscularis (P, arrowheads). According to area-adjusted cell counting in the muscularis, 59 % of iNOS+ cells are smooth muscle cells, whereas only 41 % are F4/80+ (Q). In contrast, in L-clodronate treated mice, only 7 % of iNOS-expressing cells are F4/80+; 93 % are SMA+ smooth muscle cells (Q). In a different comparison, 31 % of F4/80+ cells are iNOS-positive after DSS treatment, whereas only 4 % in the presence of L-clodronate (Q). R and S show the comparison of cell densities of F4/80, Ly6G, and iNOS positive cells in the muscularis layer in the different experimental groups. Bar charts show data for cell counting, including means and standard deviation; * $P < .05$, ** $P < .01$, *** $P < .001$. Box and whisker plots (minimum-to-maximum) show median of fold change values with 95 % confidence intervals. * $P < .05$, ** $P < .01$, *** $P < .001$.

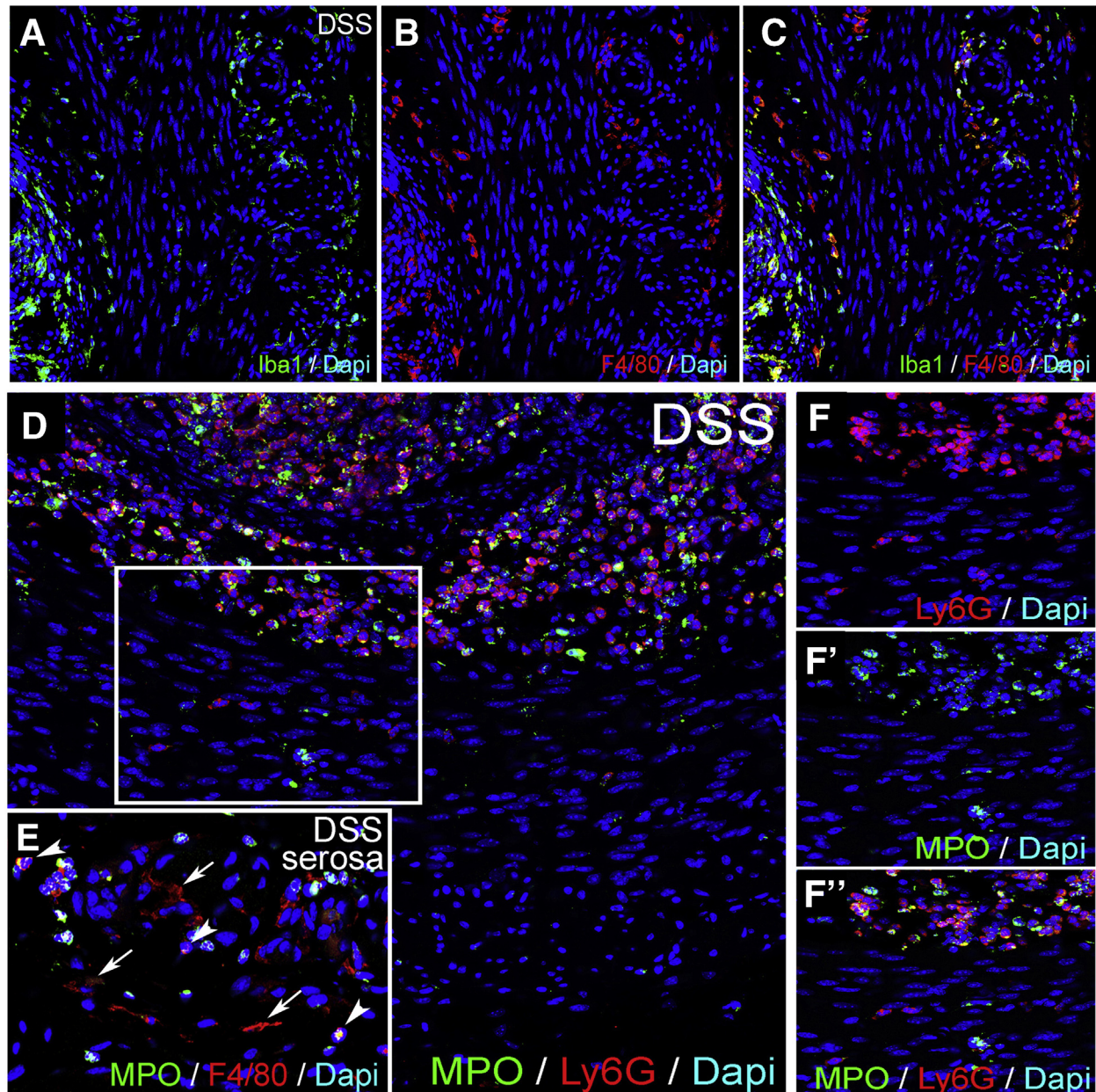


Figure 9. Iba1 and MPO expression in DSS-treated colon. Expression of Iba1 and F4/80 is co-localized in the colon of a DSS-treated mouse (A–C). Expression of MPO overlaps with Ly6G in neutrophils of the mucosa and submucosa (D), whereas some Ly6G+ cells in the muscularis propria do not express MPO (F–F’). In the serosa, ramified F4/80+ macrophages are MPO-negative (E, arrows), whereas round F4/80+ monocytes express MPO (E, arrowheads). MPO, myeloperoxidase.

horseradish peroxidase (34 kDa) and Evans blue labeled albumin (69 kDa) by Gershon and Bursztajn,²⁵ and no tracer molecules were detected around or inside the myenteric plexus after 45 minutes. This led those investigators to hypothesize the presence of a blood-myenteric plexus barrier to macromolecular diffusion. To assess the barrier function of the ganglionic basement membrane more directly, we injected FITC-dextran of a lower molecular weight (4 kDa) rather than albumin or horseradish peroxidase. This low molecular size FITC-dextran is able to leak out from myenteric plexus capillaries, leading to the interstitial accumulation of fluorescent particles in the PGS. FITC-

dextran loadings supported the observation of Gershon and Bursztajn that the outer boundary of the enteric ganglia is indeed impermeable. Thus the BMB is able to restrict the passive transport of 4 kDa particles. Interestingly, some IGMs containing FITC-dextran particles were observed in the impermeable myenteric plexus 15 minutes after MyMs acquired FITC expression. Although sensory dorsal root and autonomic ganglia include blood vessels where monocytes can exit via diapedesis directly into the neuronal tissue,⁴⁴ blood and lymphatic vessels are not present inside enteric ganglia.^{23,24} This suggests that MMs actively took up FITC-dextran particles and brought them into the myenteric

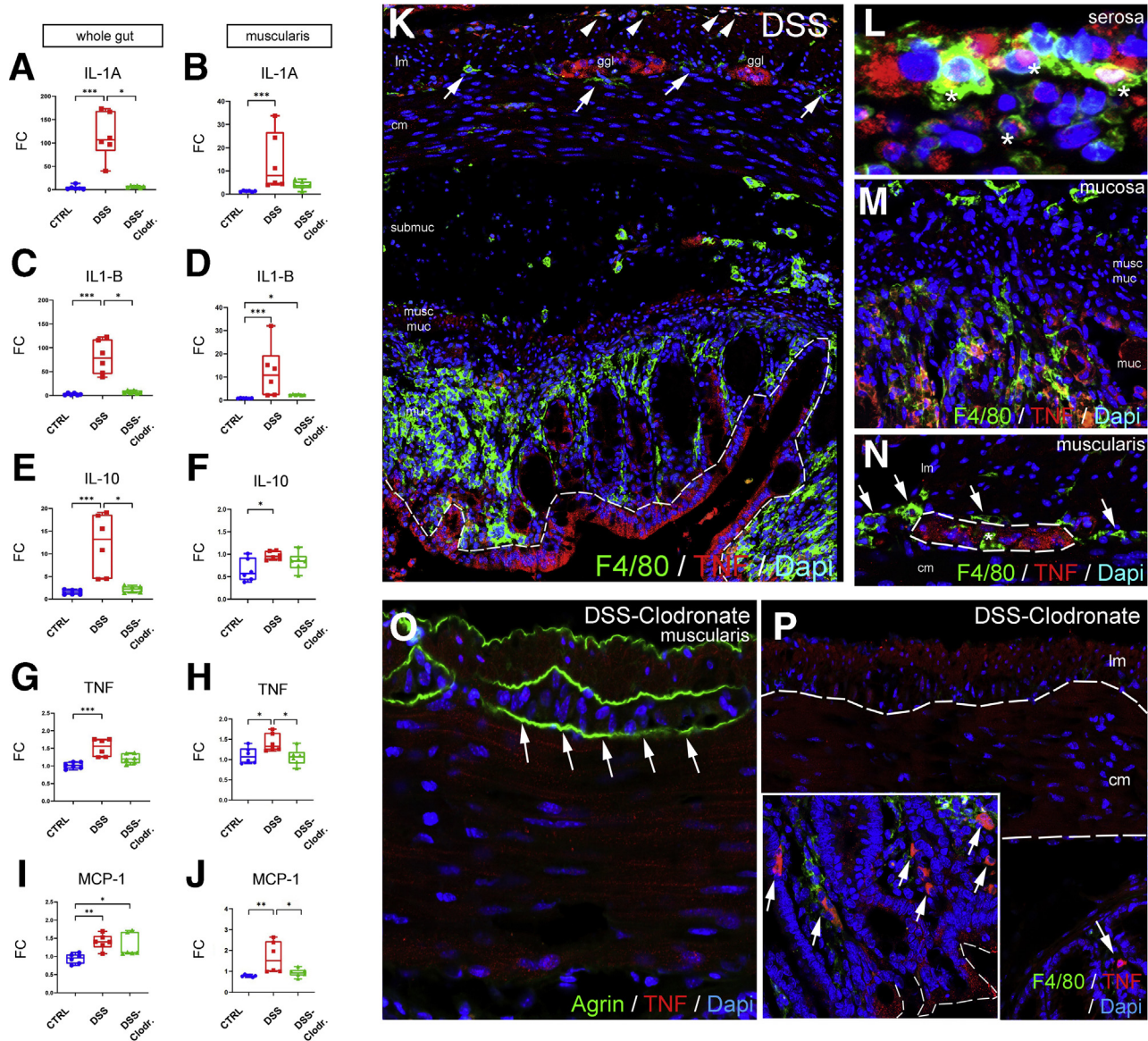


Figure 10. Macrophages are required for muscularis propria expression of proinflammatory cytokines during DSS-induced colitis. Graphs show relative RNA expression (fold change, FC) of inflammation-related biomarkers in whole gut and isolated muscularis. qPCR shows significantly higher expression of IL1A (A), IL1B (C), and IL10 (E) in the whole gut after DSS treatment as compared with control and clodronate-treated groups. In muscularis samples, IL1A (B), IL1B (D), and IL10 (F) expression is significantly increased in DSS-treated vs control) but does not reach statistical significance compared with DSS-clodronate treatment. TNF (G and H) and MCP-1 (I and J) expression is significantly increased in DSS-treated whole gut and muscularis. Immunofluorescence in DSS-treated mouse colon shows strong expression of TNF in the epithelium (K, dashed line), serosal monocytes and macrophages (L, asterisks), mucosal macrophages (M), and enteric ganglia (N, dashed line), but not in MMs (N, arrows) or IGMs (N, asterisk). With clodronate treatment, the muscularis and enteric ganglia show no immunoreactivity for TNF (O, arrows), only scattered F4/80+ macrophages (P, arrows), and clusters of epithelial cells in the mucosa (P, inset). Box and whisker plots (minimum-to-maximum) show median of fold change values with 95 % confidence intervals. * $P < .05$, ** $P < .01$, *** $P < .001$. cm, circular muscle; ggl, ganglia; lm, longitudinal muscle; muc, mucosa; musc muc, muscularis mucosa.

plexus from the PGS, indicating that MyMs traffic into the ganglia through the BMB in physiological conditions.

Although these data suggest that MMs are capable of trafficking in and out of the enteric ganglia, IGMs are unique and undergo several structural changes. Inside the ganglia, IGMs exhibit signs of cellular degeneration, including extensive cytoplasmic vacuolization and accumulation of swollen mitochondria with no morphologic signs of

apoptosis. IGMs show distinct ultrastructure from extraganglionic MyMs with an active translational machinery and Golgi apparatus. These features indicate that MyMs and IGMs may have different functions and roles in pathologic conditions. This is supported by similar phenomena in the sciatic nerve where transcriptionally unique perineurial and endoneurial macrophages are differentially activated in response to crush injury.⁴⁵

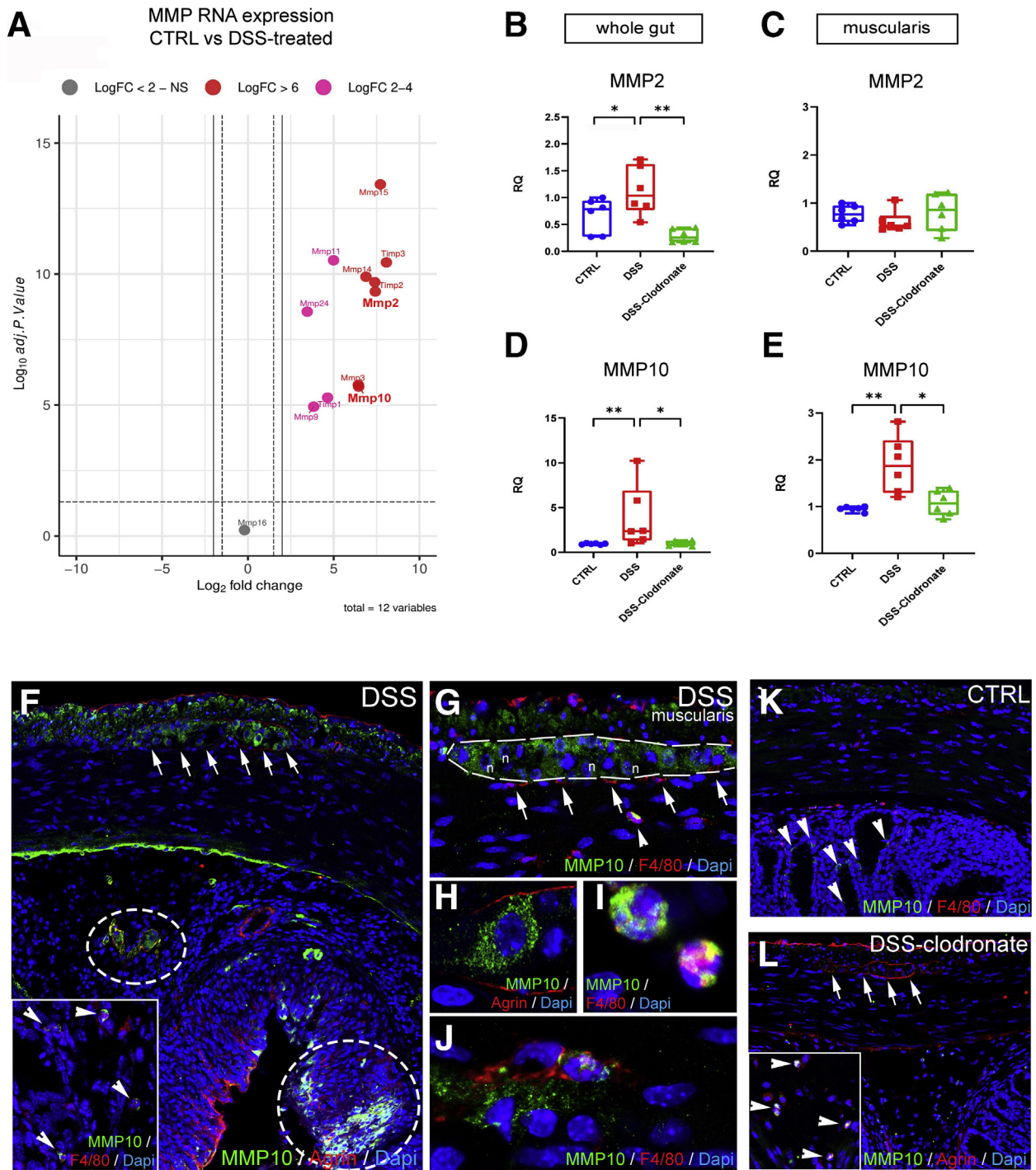


Figure 11. Secretion of MMP10 by MMs and enteric ganglia contributes to BMB disruption in DSS-induced colitis. Volcano plot shows that MMP expression is increased in DSS-treated animals compared with controls (A), including MMP2 (LogFc 7.42, $P < .001$) and MMP10 (LogFc 6.45, $P < .001$). Graphs show relative RNA expression (fold change, FC) of MMP2 and MMP10 in whole gut and isolated muscularis samples. MMP2 expression is significantly increased in whole gut of DSS-treated animals (B) but not in the muscularis (C), whereas MMP10 expression is elevated in both (D and E). MMP10 is expressed diffusely in the longitudinal muscle layer and inside enteric ganglia after DSS treatment (F, arrows). In the submucosa and mucosa, MMP10 expression co-localizes with its substrate, agrin (F, circled areas) and F4/80+ monocytes and macrophages (F, arrowheads). In the muscularis, apart from enteric neurons (G and H), F4/80+ monocytes (G, arrowhead) and scattered MMs (J) express MMP10 but not MyMs or IGMs (F, arrows). In control guts, MMP10 is not expressed in the muscularis layer (K) but only in scattered F4/80-negative cells in the mucosa (K, arrowheads). In DSS+ clodronate treated animals, no MMP10 immunopositivity is detected in enteric ganglia or in the muscularis layer (L, arrows). In the submucosa small number of F4/80+ monocytes express MMP10 (L, arrowheads). Box and whisker plots (minimum-to-maximum) show median of FC values with 95 % confidence intervals. * $P < .05$, ** $P < .01$, *** $P < .001$.

Table 1. Fold Change and Adjusted *P* Values on Volcano Plot Analysis

Gene	LogFC	Adjusted <i>P</i> value
Mmp15	7,721425488	3.78E-14
Mmp2	7,426049148	4.67E-10
Mmp14	6,880658085	1.27E-10
Mmp10	6,45768995	2.00E-06
Mmp3	6,43643922	1.71E-06
Mmp11	4,994405387	2.99E-11
Mmp9	3,836082737	1.16E-05
Mmp24	3,459050834	2.73E-09
Mmp16	-0,197007951	0.598400541
Timp3	8,072593837	3.60E-11
Timp2	7,395911406	2.05E-10
Timp1	4,645747477	5.23E-06

The presence of a subpopulation of macrophages inside the enteric ganglia is curious, and its functional importance requires elucidation. Interestingly, the immunophenotype of these IGMs is similar to that of microglial cells, including the expression of CX3CR1, Iba1, and CSF1R.^{21,46} Microglia are the predominant immune cell in the brain parenchyma and play an important role in phagocytosis, neuroprotection during ischemia and inflammation,⁴⁷ and synaptic pruning.⁴⁸ They also contribute to BBB homeostasis in steady-state and pathologic conditions.⁴⁹ The shared immunophenotype of IGMs and microglia suggests potentially parallel functions in removing dead cells and modulating inflammatory signaling in their respective nervous systems. In support of this, we observed that IGMs show active signs of phagocytosis, which is based on their subcellular characteristics on electron microscopy. This result is further reinforced by our finding that IGMs pick up FITC-dextran particles and bring them into the ganglia. It has been shown that immunolabeled MMs can contain tdTomato expression in ChAT-cre:tdTomato mice, suggesting that macrophages phagocytose enteric neurons during homeostatic maintenance of the ENS.⁵⁰ Our data support this and indicate that IGMs are a distinct phagocytic population of macrophage critical to this process.

Crosstalk between the microbiome, macrophages, and ENS is beginning to be elucidated and has implications in immunomodulation and intestinal disease.¹⁸ Studies in experimental colitis demonstrate that enteric neuroinflammation disrupts neurally regulated processes, such as intestinal motility, and results in neural hyperexcitability, local leukocyte infiltration to the enteric ganglia (plexitis), neuronal death, neurochemical plasticity, and a “reactive” glial cell phenotype.^{6,51,52} However, the mechanisms driving neuroinflammation in the gut are unknown. In our study, DSS-induced colitis resulted in significant inflammation in the muscularis propria indicated by increased expression of iNOS in macrophages and smooth muscle cells and elevated levels of inflammatory cytokines including TNF, IL1A, IL1B, and MCP-1, which is in line with other studies.^{53,54} ECM

proteins in the muscularis propria were degraded, including agrin and Col4 of the ganglionic basement membrane, which was associated with increased numbers of IGMs. This resulted in the loss of BMB integrity, which could be critical to initiating enteric neuroinflammation via infiltration of PAMPs and proinflammatory leukocytes. Our data indicate that these interactions are unlikely in physiological conditions because of BMB impermeability and may only occur after the barrier is compromised. Degradation of the barrier may allow non-resident immune cells to interact with the enteric ganglia and result in neuronal injury. Intraganglionic non-resident leukocytes, described in plexitis or ganglionitis, are observed in Crohn’s disease and may precede and contribute to the progression of inflammation.⁶ This is supported by the observation that plexitis in grossly uninfamed intestinal segments is a predictor of disease recurrence after surgery for Crohn’s disease.⁵⁵ Our data indicate that muscularis inflammation is associated with elevated levels of macrophages and neutrophils, albeit neutrophils were present in lower quantities and, unlike macrophages, did not physically interact with the ENS or constitute the leukocytes involved in plexitis.

Considering that MMs were observed to acquire a proinflammatory phenotype and exhibit enhanced penetration of the enteric ganglia during colitis, we hypothesized that BMB disruption was mediated by MMs. Macrophages were depleted using the liposome-encapsulated clodronate (L-clodronate) model, which ablates infiltrating macrophages in the intestine.⁵⁶ Co-administration of DSS and L-clodronate had several notable consequences. The severity of colitis was reduced in mice treated with L-clodronate, which is consistent with ablation of proinflammatory M1 polarized macrophages.³³ M1 polarization is not specific to the mucosa, because proinflammatory MMs are also observed during colitis,¹¹ albeit our data indicate that despite the induction of the M1 marker iNOS, the expression of the M2-associated markers, ARG-1 and CD163, is maintained during inflammation in the intestine. Nevertheless, increases in the number of MMs and IGMs and the extent of M1-polarization in colitis were attenuated after L-clodronate treatment. This correlated with the preservation of ECM patterning and the amelioration of BMB permeability, thus confirming that MMs and IGMs play a pivotal role in the inflammation-associated ECM degradation and BMB injury that occur during colitis. This further indicates that, like microglia and the BBB,⁴⁹ MMs can contribute to BMB permeability in pathologic conditions.

Intestinal inflammation is known to induce expression of ECM remodeling MMPs in macrophages.⁵⁷ These enzymes are responsible for BBB failure in chronic neurodegenerative disorders and may explain the effects of MMs on BMB degradation.⁵⁸ Here, we showed that MMP10 is specifically overexpressed in the muscularis after DSS. MMP10 was expressed by MMs and returned to baseline levels in the muscularis with concurrent L-clodronate treatment. Interestingly, we identified that enteric neurons also secreted MMP10 in mice with colitis. Likewise, the major source of elevated TNF in the muscularis originated from the enteric ganglia. The expression of MMP10 and TNF in the myenteric

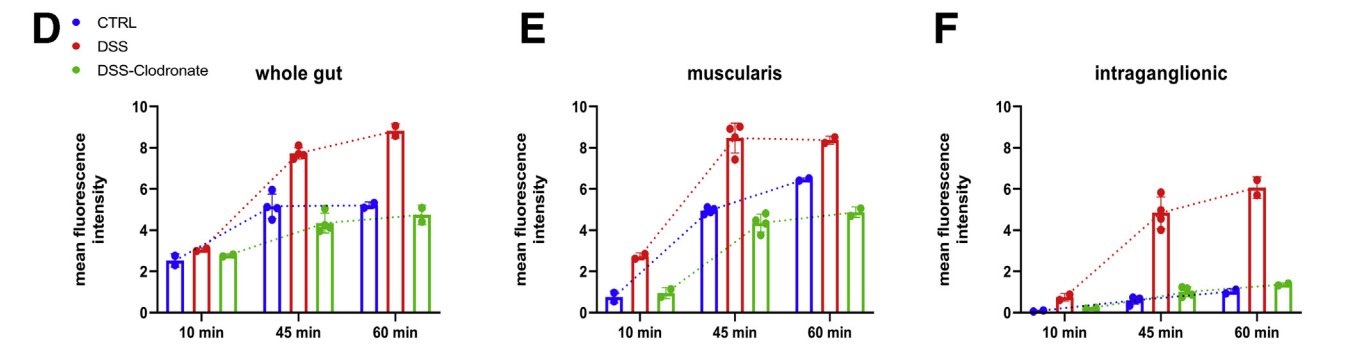
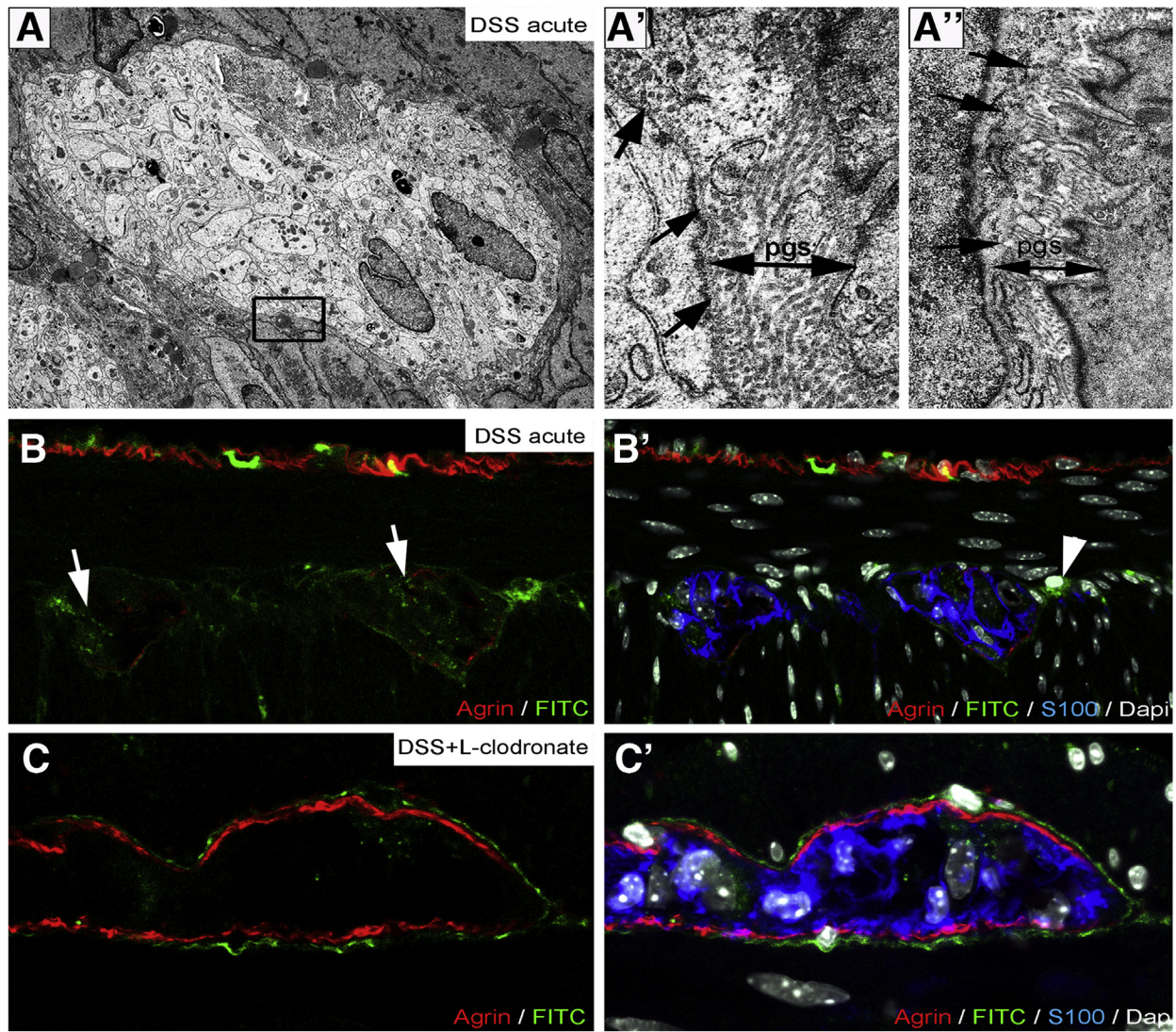


Figure 12. DSS colitis is associated with macrophage-dependent structural and functional disruption of the BMB. Electron microscopy of DSS-treated colon (A) reveals partial disruption (A', arrows) or complete absence (A'', arrows) of periganglionic basement membrane. PGS is dense and closely packed with collagen fibers (A'-A'', double arrows). 60 minutes after administration of FITC-dextran to DSS-treated animals leads to FITC accumulation in the enteric ganglia (B-B') and MyMs (B', arrowhead). Clodronate treatment prevents this, leaving FITC-dextran particles accumulating in the PGS surrounding the ganglia (C-C'). D, E, and F show the change in mean fluorescent intensity 10, 45, and 60 minutes after FITC-dextran injections in whole gut (D), muscularis (E), and enteric ganglia (F).

ganglia was dependent on the presence of macrophage. These data indicate that although degradation of the ECM, BMB permeability, and neuroinflammation are macrophage-

dependent processes, secondary responses from the enteric neurons and glia may contribute to barrier degradation and the inflammatory milieu.

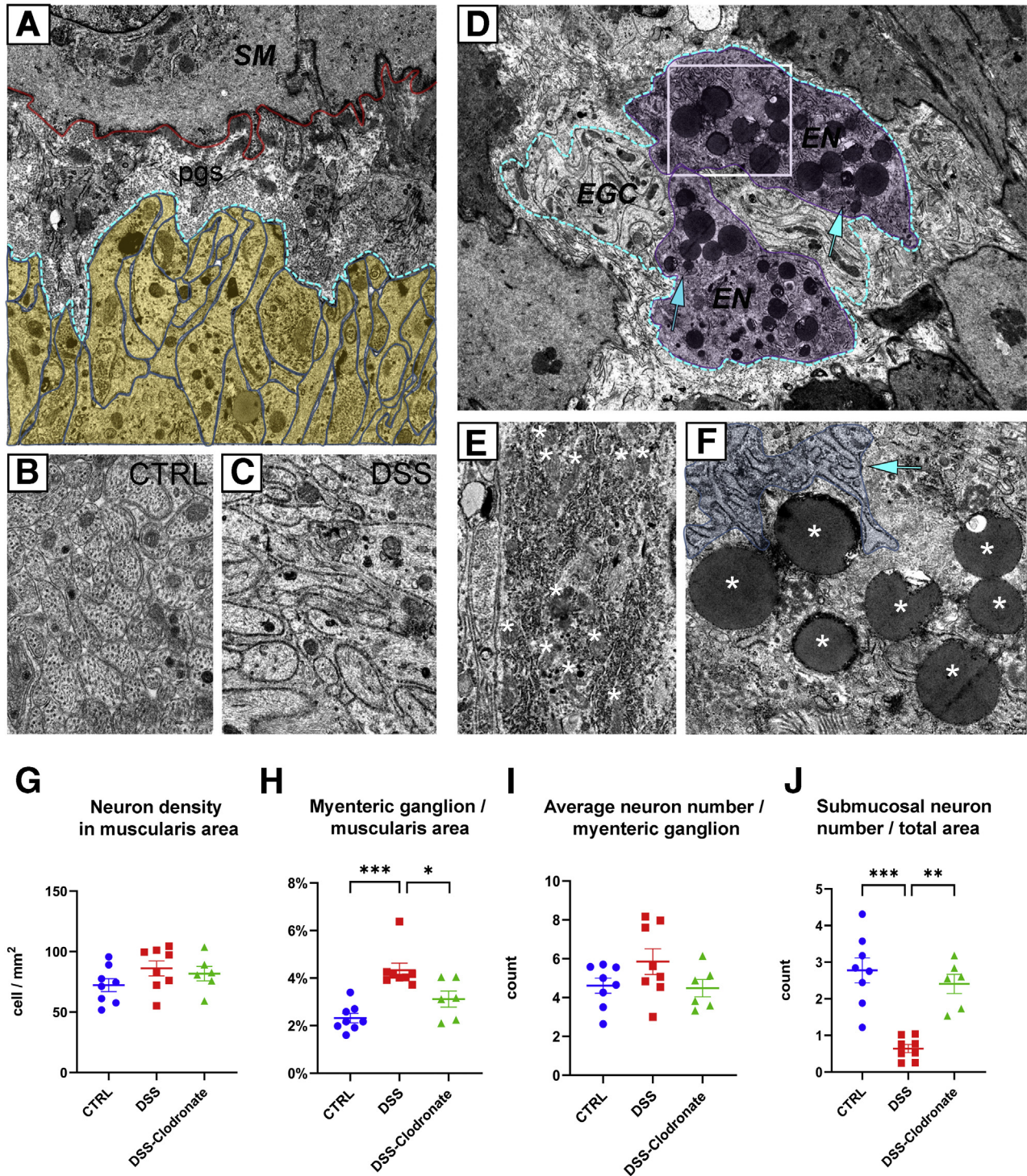


Figure 13. DSS colitis is associated with enteric neuroinflammation, including neural hypertrophy, glial swelling, and submucosal plexus degeneration. Electron microscopy shows swollen glial end-feet arranged perpendicularly (A, yellow shaded area) to the border of enteric ganglion (A, blue dashed line). B and C show enteric glial morphology in control vs DSS-treated animals. Enteric neurons (D, magenta shaded area) after DSS treatment accumulate lipid droplets (D, arrows; F, asterisks) and mitochondria (E, asterisks) and exhibit a hyperplastic rough ER (E and F, arrow). Number of enteric neurons is unchanged after DSS (G), but their total surface area adjusted to total muscularis area increases significantly and is reversed with L-clodronate injection (H). Average neuron number per myenteric ganglion is unchanged after DSS colitis, whereas number of submucosal neurons decreases significantly (J), and this is reversed with L-clodronate treatment (J). Scatter diagrams show data for morphometry and cell counting, including means and standard deviation; * $P < .05$, ** $P < .01$, *** $P < .001$.

Our data reveal that macrophage-mediated degradation of the ECM and the basement membrane surrounding the enteric ganglia disrupts its physiological barrier, eliminates the separation of the intra- and extra-ganglionic compartments, and allows inflammatory stimuli to access the myenteric plexus. This process offers a mechanism for the onset of neuroinflammation in chronic colitis and other GI pathologies with acquired ENS dysfunction.

Materials and Methods

Animals

Adult CX3CR1^{+/GFP} (C57BL/6) mice and wild-type C57BL/6 mice (80–120 days old) were obtained from the Medical Gene Technology Unit (Specific Pathogen Free, SPF level) at the Institute of Experimental Medicine, Budapest. In CX3CR1^{+/GFP} knock in-knock out mice (CX3CR1^{GFP}), cells that express fractalkine receptor are EGFP+, whereas the presence of one normal allele retains their chemotactic function.⁵⁹ Animals were housed at the Minimal Disease level, 3–5/cage under controlled environmental conditions: 21°C ± 1°C temperature, 65 % humidity, 12-hour light-dark cycle, with free access to food and water. PLP-1^{GFP} mice (C57BL/6) (80 days old) were provided by Dr Hans-Christian Reinecker, Massachusetts General Hospital, Boston. All procedures were conducted in accordance with the guidelines set by the European Communities Council (86/609/EEC/2 and 2010/63 Directives of European Community), and the protocol was approved by the Institutional Animal Care and Use Committee of the Institute of Experimental Medicine, Budapest (permit number: PEI/001/29-4/2013).

Histologic Procedures

For immunofluorescence studies, colon samples of CX3CR1^{GFP}, PLP1^{GFP}, and wild-type control, DSS-treated and DSS-clodronate treated C57BL/6 mice were fixed in 4 % paraformaldehyde in phosphate-buffered saline (PBS) (PFA) for 24 hours. Two-cm-long proximal colon samples from CX3CR1^{GFP} mice were removed 2.5 cm distally from the ileocecal junction. For distal colon samples the last 2 cm was removed from the abdominal part of the large intestine in every mouse breed. After extensive washing in PBS the medium was changed to 7.5 % gelatin containing 15 % sucrose at 37°C for 2 hours, and the tissues were rapidly frozen at 60°C in isopentane (Sigma-Aldrich, St Louis, MO). Frozen sections were cut at 5 μm for super-resolution microscopy (STED imaging) and at 10 μm for laser scanning confocal microscopy, collected on poly-L-lysine-coated slides (Sigma-Aldrich).

Electron Microscopy

For electron microscopy studies, gut samples from control and DSS-treated C57BL/6 mice were placed in 4 % buffered glutaraldehyde for 72 hours. After washing in PBS, postfixation was made in 1 % osmium tetroxide for 2 hours. After being rinsed 3 times in PBS, the tissue samples were dehydrated in graded ethanol and embedded in epoxy resin (Polysciences Inc, Warrington, PA) using propylene oxide.

Ultrathin sections were contrasted with uranyl acetate and lead citrate and examined using H-7600 Hitachi (Tokyo, Japan) electron microscope.

Pre-embedding Immunocytochemistry on Semithin Sections

Fifty-μm frozen sections were made from gelatin-embedded specimens using a Shandon cryostat, placed in 12-well plates, and permeabilized with 0.1 % Triton-X solution for 30 minutes at 38°C. Sections were incubated with the first primary antibody (anti-agrin) diluted in 1 % PBS-bovine serum albumin for 24 hours, followed by first secondary antibody anti-goat immunoglobulin G (Vector Labs, Burlingame, CA) for 24 hours and avidin-biotinylated peroxidase complex for 6 hours (Vectastain Elite ABC kit; Vector Labs). Endogenous peroxidase activity was quenched with 1 % hydrogen peroxide (Sigma-Aldrich). Antibody binding was visualized with 0.04 % 3,3'-diaminobenzidine (Sigma-Aldrich) and 0.03 % H₂O₂ for 10 minutes. Extensive washing in PBS for 3 hours was followed by addition of the second primary antibody (anti-GFP) for 24 hours and second secondary antibody AP anti-rabbit immunoglobulin G (Vector Labs) for 24 hours. Endogenous alkaline phosphatase activity was quenched with 5 % levamisole solution. Antigen binding was revealed by VectaRed AP kit (Vector Labs). After immunocytochemistry, samples were postfixed in 4 % PFA and 0.1 % glutaraldehyde for 48 hours and 1 % osmium tetroxide (Polysciences Inc) for 10 minutes. After dehydration in graded ethanol, tissue blocks were embedded in Polybed/Araldite6500 (Polysciences Inc), and 1-μm semithin sections were counterstained with toluidine blue.

Immunofluorescence and Image Analysis

For immunofluorescence staining, primary antibodies were diluted in 1 % PBS-bovine serum albumin. Frozen sections were incubated with primary antibodies for agrin (R&D Systems, Minneapolis, MN; #AF550), Hu (Abcam, Cambridge, MA; #96474), CD45 (BioLegend, San Diego, CA; #30F11), anti-GFP (R&D Systems; #AF4240), CD11b (Bio-Rad, Hercules, CA; #M1/70.15), CSF1R (Invitrogen, Waltham, MA; #PA5-25974), F4/80(BM8) (Invitrogen; #41-4801-82), Iba1 (Invitrogen; #PA5-27436), NCAM (Invitrogen; #PA5-78402), Col4 (Abcam; #236640) and S100A1 (Invitrogen; #PA1-932), Ly6G (Abcam; #25377), MPO (R&D Systems; #AF3667), CD45 (BioLegend; #103102), G-SMA (SBC; #65638), TNF (Abcam; #183218), MMP2 (Invitrogen; #PA5-115583), and MMP10 (Invitrogen; #PA5-79677) overnight at 4°C, followed by secondary antibodies (Alexa Fluor 647, 546, and 488 conjugated anti-rabbit immunoglobulin G; Alexa Fluor 647 and 555 conjugated anti-goat immunoglobulin G; Alexa Fluor 488 and 594 conjugated anti-rat; Invitrogen) for 1 hour. Cell nuclei were visualized by DAPI. Sections were covered with aqueous Poly/Mount (Polyscience Inc) and examined with a Zeiss LSM 780 laser-scanning confocal microscope (Zeiss, Oberkochen) or Nikon Eclipse Ti2-E inverted microscope with an Abberior STED super resolution imaging platform. Images were compiled by

ImageJ and Adobe Photoshop CS6 (San Diego, CA) software package.

Cell Counting and Morphometry

Images of sections from distal and proximal segments of wild-type C57BL/6 and CX3CR1^{GFP} mouse colons were captured with a Zeiss LSM 780 laser-scanning confocal microscope. For cell counting and morphometry, tile scans of 9 (3 horizontal, 3 vertical) \times 20 magnification images of 2MP were compiled by the ZEN software package to include the total cross-sectional area of the observed gut sample. For every mouse gut sample 6 separate sections were scanned, distributed vertically in the frozen gelatin block with at least 200 μ m between each section. Morphometry for cell density measurements was carried out by the ZEN software package by manual annotation of measured areas (muscularis and myenteric ganglion area). Ganglionic borders were determined on the basis of anti-agrin or anti-S100 immunostaining. Cell counting of F4/80+ macrophages, Ly6G+ neutrophils, iNOS+ M1-polarized macrophages, and Hu+ enteric neurons in different anatomic locations were compiled by a systematic quantitative method based on software-assisted, manual cell counting by 2 independent observers with the aid of the “cell counter” plugin of the ImageJ software package. Only cells with visible DAPI-stained nuclei were included in the calculations. Square micrometers (μ m²) were converted to square millimeters (mm²) for calculation of cell density parameters in statistical analyses. Summary of cell counting and morphometry data is shown in the [Supplementary Material](#).

Quantitative Real-Time Polymerase Chain Reaction

For qPCR analysis muscularis externa separated mechanically from mucosal layers of distal colon were washed in DEPC-PBS and stored in -80° C freezer. Frozen tissue samples were homogenized in TRI reagent solution (Ambion, Austin, TX), and total RNA was isolated with a QIAGEN RNeasy minikit (Qiagen, Hilden, Germany)

according the manufacturers' instructions. To eliminate genomic DNA contamination, DNase I treatment was used, and 100 μ L of RNase-free DNase I (1 U of DNase) (Thermo Scientific, Waltham, MA) solution was added. Sample quality control and the quantitative analysis were carried out by NanoDrop 2000 (Thermo Scientific). Amplification was not detected in the RT-minus controls. The cDNA synthesis was performed with a high-capacity cDNA reverse transcription kit (Applied Biosystems, Waltham, MA). Primers for the comparative Ct experiments were designed by the Primer Express 3.0 program and Primer-BLAST software. The primers (Microsynth AG, Balgach, Switzerland) were used in the real-time PCR with Fast EvaGreen qPCR master mix (Biotium, Fremont, CA) on an ABI StepOnePlus instrument (Applied Biosystems, Waltham, MA) and are listed in [Table 2](#). The gene expression was analyzed by the ABI StepOne 2.3 program. The amplicon was tested by melt curve analysis on an ABI StepOnePlus PCR instrument. Experiments were normalized to GAPDH expression.

DSS Colitis and Liposomal Clodronate Treatment

C57BL/6 male mice (100–120 days old) were treated with drinking water containing 2.5 % DSS (MP Biomedicals, Solon, OH; #160110) for 7 days.⁶⁰ During treatment, disease activity index and weight were recorded. At the end of the experiment, animals were anesthetized and killed by cervical dislocation (n = 6). Colon lengths were measured and samples fixed in 4 % PFA.

For clodronate treatment, mice on the third day of DSS treatment were injected via tail vein (n = 6) with 300 μ L of liposomal clodronate suspension (Clodronate Liposomes dissolved in PBS; LMS Consult GmbH&Co, Brigachthal, Germany) to deplete the macrophages.⁶¹ Animals were relocated to the animal facility, where DSS administration continued for 4 additional days. Control animals were injected with saline as vehicle (n = 6).

FITC-Dextran Assays

For permeability assays, 300 μ L of FITC-dextran (4 kDa FITC-dextran; Sigma-Aldrich, #60842-46-8) derived from

Table 2. Primer Sequences Used in qRT PCR Reactions

Gene	Forward	Reverse
GAPDH	TGACGTGCCGCCTGGAGAAA	AGTGTAGCCCAAGATGCCCTTCAG
TNF α	CAGCCGATGGGTTGTACCTT	GGCAGCCTTGTGCCTTGA
IL-1A	CCATAACCCATGATCTGGAAGAG	GCTTCATCAGTTTGTATCTCAAATCAC
IL-1B	GCCTCGTGCTGTCGGACCCA	TGAGGCCCAAGGCCACAGGT
IL-10	AGTGAGAAGCTGAAGACCCTCAGG	TTCATGGCCTTGTAGACACCTTGGT
ARG-1	GTCTGGCAGTTGGAAGCATCT	GCATCCACCCAATGACACA
MCP-1	CCAGCACCAGCACCAGCCAA	TGGATGCTCCAGCCGGCAAC
Ly6g	GTGGTCCTACTGTGTGCAGAA	CTCAGGTGGACCCCAATAC
MMP2	GCCCCATGAAGCCTTGT	ATAGCGTCTCGGGACAGAA
MMP10	AGACCTGAGACCCAGACAA	CTGCGCCAGAAGTACCTGTC
CD163	AGGTTTCTTTGTTGTGGCTGTG	CATTTCTCCAGGAGCGTTAGTG
iNOS	TGGTGAAGGGACTGAGCTGTT	TCCGTTCTTGCAGTTGACT

Leuconostoc mesenteroides, diluted 5 mg/mL in saline was administered via tail vein to 100-day-old healthy (n = 7), DSS-treated (n = 4), and DSS- and clodronate-treated (n = 4) mice, as previously described.⁶² Animals were killed 10 minutes (n = 2), 45 minutes (n = 4), or 60 minutes (n = 2) after injection. Apart from distal colon, liver and cerebellum were fixed from mice in the control group in 4 % PFA.

Mean Fluorescent Intensity Measurement

For mean fluorescent intensity measurements of FITC-dextran, tile scans of 9 (3 horizontal, 3 vertical) ×20 magnification images of 2MP were performed by the ZEN software package with a Zeiss LSM 780 laser-scanning confocal microscope. For every gut sample, 2 separate sections were scanned to include the whole cross-sectional area of the observed distal colon segment. On each tile scan, areas corresponding to gut compartments (whole gut, muscularis, total intraganglionic area; Figure 8D–F) were annotated manually. For the normalized measurement of area-adjusted mean fluorescent intensity, identical laser-intensity adjustments were set for the scanning of each specimen.

Statistical Analyses

For analyzing morphometric data we tested normality first with the Shapiro-Wilk test. Bartlett's test was used for testing homogeneity of variances. In case of homoscedasticity, we performed Student *t* test; otherwise Welch *t* test was performed. When we compared 3 groups by 2 factors, we used ordinary two-way analysis of variance (Figure 5, R and S). For analyzing PCR datasets (Figure 5A–H, Figure 6A–J, Figure 7B–E), we used Kruskal-Wallis test followed by uncorrected Dunn's multiple comparison test. Data were analyzed and graphs generated with GraphPad Prism 9.1.1 for Windows, GraphPad Software, San Diego, CA. *P* < .05 was considered significant: **P* < .05, ***P* < .01, ****P* < .001. Data pre-processing from a publicly available RNAseq database (accession number: PRJNA687627) was carried out with the R software package. Differential gene expression panels were filtered for MMPs (Table 1) and compiled with *ggrepel* (0.8.2), whereas volcano plot visualization was generated with *EnhancedVolcano* (1.8.0) R packages.

References

1. Goldstein AM, Hofstra RM, Burns AJ. Building a brain in the gut: development of the enteric nervous system. *Clinical Genetics* 2013;83:307–316.
2. Muller PA, Koscsó B, Rajani GM, Stevanovic K, Berres ML, Hashimoto D, Mortha A, Leboeuf M, Li XM, Mucida D, Stanley ER, Dahan S, Margolis KG, Gershon MD, Merad M, Bogunovic M. Crosstalk between muscularis macrophages and enteric neurons regulates gastrointestinal motility. *Cell* 2014;158:300–313.
3. Geboes K, Collins S. Structural abnormalities of the nervous system in Crohn's disease and ulcerative colitis. *Neurogastroenterol Motil* 1998;10:189–202.
4. Belai A, Boulos PB, Robson T, Burnstock G. Neurochemical coding in the small intestine of patients with Crohn's disease. *Gut* 1997;40:767–774.
5. De Giorgio R, Guerrini S, Barbara G, Stanghellini V, De Ponti F, Corinaldesi R, Moses PL, Sharkey KA, Mawe GM. Inflammatory neuropathies of the enteric nervous system. *Gastroenterology* 2004;126:1872–1883.
6. Stavely R, Abalo R, Nurgali K. Targeting enteric neurons and plexitis for the management of inflammatory bowel disease. *Current Drug Targets* 2020;21:1428–1439.
7. BainCC Schridde A. Origin, differentiation, and function of intestinal macrophages. *Frontiers in Immunology* 2018;9:2733.
8. Dóra D, Fejszák N, Goldstein AM, Minkó K, Nagy N. Ontogeny of ramified CD45 cells in chicken embryo and their contribution to bursal secretory dendritic cells. *Cell Tissue Res* 2017;368:353–370.
9. Bogunovic M, Ginhoux F, Helft J, Shang L, Hashimoto D, Greter M, Liu K, Jakubzick C, Ingersoll MA, Leboeuf M, Stanley ER, Nussenzweig M, Lira SA, Randolph GJ, Merad M. Origin of the lamina propria dendritic cell network. *Immunity* 2009;31:513–525.
10. Ozaki H, Kawai T, Shuttleworth CW, Won KJ, Suzuki T, Sato K, Horiguchi H, Hori M, Karaki H, Torihashi S, Ward SM, Sanders KM. Isolation and characterization of resident macrophages from the smooth muscle layers of murine small intestine. *Neurogastroenterol Motil* 2004;16:39–51.
11. Kinoshita K, Horiguchi K, Fujisawa M, Kobirumaki F, Yamato S, Hori M, Ozaki H. Possible involvement of muscularis resident macrophages in impairment of interstitial cells of Cajal and myenteric nerve systems in rat models of TNBS-induced colitis. *Histochem Cell Biol* 2007;127:41–53.
12. Gabella G. Ultrastructure of the nerve plexuses of the mammalian intestine: the enteric glial cells. *Neuroscience* 1981;6:425–436.
13. Cook RD, Burnstock G. The ultrastructure of Auerbach's plexus in the guinea-pig: II—non-neuronal elements. *Journal of Neurocytology* 1976;5:195–206.
14. Komuro T, Baluk P, Burnstock G. An ultrastructural study of neurons and non-neuronal cells in the myenteric plexus of the rabbit colon. *Neuroscience* 1982;7:1797–1806.
15. Mikkelsen HB. Macrophages in the external muscle layers of mammalian intestines. *Histol Histopathol* 1995;10:719–736.
16. Phillips RJ, Powley TL. Macrophages associated with the intrinsic and extrinsic autonomic innervation of the rat gastrointestinal tract. *Auton Neurosci* 2012;169:12–27.
17. Avetisyan M, Rood JE, Huerta Lopez S, Sengupta R, Wright-Jin E, Dougherty JD, Behrens EM, Heuckeroth RO. Muscularis macrophage development in the absence of an enteric nervous system. *Proc Natl Acad Sci U S A* 2018;115:4696–4701.
18. Gabanyi I, Muller PA, Feighery L, Oliveira TY, Costa-Pinto FA, Mucida D. Neuro-immune phages. *Cell* 2016;164:378–391.
19. Shaw TN, Houston SA, Wemyss K, Bridgeman HM, Barbera TA, Zangerle-Murray T, Strangward P, Ridley A,

- Wang P, Tamoutounour S, Allen JE, Konkel JE, Grainger JR. Tissue-resident macrophages in the intestine are long lived and defined by Tim-4 and CD4 expression. *J Exp Med* 2018;215:1507–1518.
20. De Schepper S, Verheijden S, Aguilera-Lizarraga J, Viola MF, Boesmans W, Stakenborg N, Voytyuk I, Schmidt I, Boeckx B, Dierckx de Casterlé I, Baekelandt V, Gonzalez Dominguez E, Mack M, Depoortere I, De Strooper B, Sprangers B, Himmelreich U, Soenen S, Williams M, Vanden Berghe P, Jones E, Lambrechts D, Boeckxstaens G. Self-maintaining gut macrophages are essential for intestinal homeostasis. *Cell* 2018;175:400–415.e13.
 21. Dora D, Arciero E, Hotta R, Barad C, Bhave S, Kovacs T, Balic A, Goldstein AM, Nagy N. Intraganglionic macrophages: a new population of cells in the enteric ganglia. *J Anat* 2018;233:401–410.
 22. Banks WA, Robinson SM. Minimal penetration of lipopolysaccharide across the murine blood-brain barrier. *Brain Behav Immunity* 2010;24:102–109.
 23. Gabella G. Fine structure of the myenteric plexus in the guinea-pig ileum. *J Anat* 1972;111(Pt 1):69–97.
 24. Kiernan JA. Vascular permeability in the peripheral autonomic and somatic nervous systems: controversial aspects and comparisons with the blood-brain barrier. *Microsc Res Tech* 1996;35:122–136.
 25. Gershon MD, Bursztajn S. Properties of the enteric nervous system: limitation of access of intravascular macromolecules to the myenteric plexus and muscularis externa. *J Comp Neurol* 1978;180:467–488.
 26. Akbareian SE, Nagy N, Steiger CE, Mably JD, Miller SA, Hotta R, Molnar D, Goldstein AM. Enteric neural crest-derived cells promote their migration by modifying their microenvironment through tenascin-C production. *Dev Biol* 2013;382:446–456.
 27. Soret R, Mennetrey M, Bergeron KF, Dariel A, Neunlist M, Grunder F, Faure C, Silversides DW, Pilon N; Ente-Hirsch Study Group. A collagen VI-dependent pathogenic mechanism for Hirschsprung's disease. *J Clin Invest* 2015;125:4483–4496.
 28. Nagy N, Barad C, Hotta R, Bhave S, Arciero E, Dora D, Goldstein AM. Collagen 18 and agrin are secreted by neural crest cells to remodel their microenvironment and regulate their migration during enteric nervous system development. Cambridge, England: Development, 2018:145.
 29. Mikkelsen HB, Huizinga JD, Larsen JO, Kirkeby S. Ionized calcium-binding adaptor molecule 1 positive macrophages and HO-1 up-regulation in intestinal muscularis resident macrophages. *Anat Rec* 2007;300:1114–1122.
 30. Rao M, Nelms BD, Dong L, Salinas-Rios V, Rutlin M, Gershon MD, Corfas G. Enteric glia express proteolipid protein 1 and are a transcriptionally unique population of glia in the mammalian nervous system. *Glia* 2015; 63:2040–2057.
 31. Waddell LA, Lefevre L, Bush SJ, Raper A, Young R, Lisowski ZM, McCulloch M, Muriuki C, Sauter KA, Clark EL, Irvine KM, Pridans C, Hope JC, Hume DA. ADGRE1 (EMR1, F4/80) is a rapidly-evolving gene expressed in mammalian monocyte-macrophages. *Frontiers in Immunology* 2018;9:2246.
 32. MacDonald TT, Monteleone I, Fantini MC, Monteleone G. Regulation of homeostasis and inflammation in the intestine. *Gastroenterology* 2011;140:1768–1775.
 33. Bain CC, Scott CL, Uronen-Hansson H, Gudjonsson S, Jansson O, Grip O, Williams M, Malissen B, Agace WW, Mowat AM. Resident and pro-inflammatory macrophages in the colon represent alternative context-dependent fates of the same Ly6Chi monocyte precursors. *Mucosal Immunology* 2013;6:498–510.
 34. Lissner D, Schumann M, Batra A, Kredel LI, Kühl AA, Erben U, May C, Schulzke JD, Siegmund B. Monocyte and M1 macrophage-induced barrier defect contributes to chronic intestinal inflammation in IBD. *Inflamm Bowel Dis* 2015;21:1297–1305.
 35. Zhu W, Yu J, Nie Y, Shi X, Liu Y, Li F, Zhang XL. Disequilibrium of M1 and M2 macrophages correlates with the development of experimental inflammatory bowel diseases. *Immunol Invest* 2014;43:638–652.
 36. Mills CD, Kincaid K, Alt JM, Heilman MJ, Hill AM. M-1/M-2 macrophages and the Th1/Th2 paradigm. *J Immunol* 2000;164:6166–6173.
 37. Ferenczi S, Solymosi N, Horváth I, Szeőcs N, Grózer Z, Kuti D, Juhász B, Winkler Z, Pankotai T, Sükösd F, Stágel A, Paholcsek M, Dóra D, Nagy N, Kovács KJ, Zononi I, Szallasi Z. Efficient treatment of a preclinical inflammatory bowel disease model with engineered bacteria. *Mol Ther* 2020;20:218–226.
 38. O'Shea NR, Smith AM. Matrix metalloproteases role in bowel inflammation and inflammatory bowel disease: an up to date review. *Inflamm Bowel Dis* 2014;20:2379–2393.
 39. Nakazawa E, Ishikawa H. Ultrastructural observations of astrocyte end-feet in the rat central nervous system. *Journal of Neurocytology* 1998;27:431–440.
 40. Rubin LL, Barbu K, Bard F, Cannon C, Hall DE, Horner H, Janatpour M, Liaw C, Manning K, Morales J. Differentiation of brain endothelial cells in cell culture. *Ann N Y Acad Sci* 1991;633:420–425.
 41. Morris AW, Sharp MM, Albargothy NJ, Fernandes R, Hawkes CA, Verma A, Weller RO, Carare RO. Vascular basement membranes as pathways for the passage of fluid into and out of the brain. *Acta Neuropathologica* 2016;131:725–736.
 42. Barber AJ, Lieth E. Agrin accumulates in the brain microvascular basal lamina during development of the blood-brain barrier. *Dev Dyn* 1997;208:62–74.
 43. Steiner E, GU Enzmann, Lyck R, Lin S, Rüegg MA, Kröger S, Engelhardt B. The heparan sulfate proteoglycan agrin contributes to barrier properties of mouse brain endothelial cells by stabilizing adherens junctions. *Cell Tissue Res* 2014;358:465–479.
 44. Monaco S, Gehrmann J, Raivich G, Kreutzberg GW. MHC-positive, ramified macrophages in the normal and injured rat peripheral nervous system. *Journal of Neurocytology* 1992;21:623–634.
 45. Ydens E, Amann L, Asselbergh B, Scott CL, Martens L, Sichien D, Mossad O, Blank T, De Prijck S, Low D, Masuda T, Saeys Y, Timmerman V, Stumm R, Ginhoux F,

- Prinz M, Janssens S, Guilliams M. Profiling peripheral nerve macrophages reveals two macrophage subsets with distinct localization, transcriptome and response to injury. *Nat Neurosci* 2020;23:676–689.
46. Verheijden S, De Schepper S, Boeckxstaens GE. Neuron-macrophage crosstalk in the intestine: a "microglia" perspective. *Frontiers in Cellular Neuroscience* 2015;9:403.
 47. Szalay G, Martinecz B, Lénárt N, Környei Z, Orsolits B, Judák L, Császár E, Fekete R, West BL, Katona G, Rózsa B, Dénes Á. Microglia protect against brain injury and their selective elimination dysregulates neuronal network activity after stroke. *Nature Communications* 2016;7:11499.
 48. Ji K, Akgul G, Wollmuth LP, Tsrirka SE. Microglia actively regulate the number of functional synapses. *PLoS One* 2013;8:e56293.
 49. Haruwaka K, Ikegami A, Tachibana Y, Ohno N, Konishi H, Hashimoto A, Matsumoto M, Kato D, Ono R, Kiyama H, Moorhouse AJ, Nabekura J, Wake H. Dual microglia effects on blood brain barrier permeability induced by systemic inflammation. *Nature Communications* 2019;10:5816.
 50. Kulkarni S, Micci MA, Leser J, Shin C, Tang SC, Fu YY, Liu L, Li Q, Saha M, Li C, Enikolopov G, Becker L, Rakhilin N, Anderson M, Shen X, Dong X, Butte MJ, Song H, Southard-Smith EM, Kapur RP, Bogunovic M, Pasricha PJ. Adult enteric nervous system in health is maintained by a dynamic balance between neuronal apoptosis and neurogenesis. *Proc Natl Acad Sci U S A* 2017;114:E3709–E3718.
 51. Pochard C, Coquenorge S, Freyssinet M, Naveilhan P, Bourreille A, Neunlist M, Rolli-Derkinderen M. The multiple faces of inflammatory enteric glial cells: is Crohn's disease a gliopathy? *Am J Physiol Gastrointest Liver Physiol* 2018;315:G1–G11.
 52. Spear ET, Mawe GM. Enteric neuroplasticity and dysmotility in inflammatory disease: key players and possible therapeutic targets. *Am J Physiol Gastrointest Liver Physiol* 2019;317:G853–G861.
 53. Kalff JC, Schraut WH, Billiar TR, Simmons RL, Bauer AJ. Role of inducible nitric oxide synthase in postoperative intestinal smooth muscle dysfunction in rodents. *Gastroenterology* 2000;118:316–327.
 54. Wehner S, Buchholz BM, Schuchtrup S, Rocke A, Schaefer N, Lysson M, Hirner A, Kalff JC. Mechanical strain and TLR4 synergistically induce cell-specific inflammatory gene expression in intestinal smooth muscle cells and peritoneal macrophages. *Am J Physiol Gastrointest Liver Physiol* 2010;299:G1187–G1197.
 55. Decousus S, Boucher AL, Joubert J, Pereira B, Dubois A, Goutorbe F, Déchelotte PJ, Bommelaer G, Buisson A. Myenteric plexitis is a risk factor for endoscopic and clinical postoperative recurrence after ileocolonic resection in Crohn's disease. *Dig Liver Dis* 2016;48:753–758.
 56. Zhao A, Urban JF Jr, Anthony RM, Sun R, Stiltz J, van Rooijen N, Wynn TA, Gause WC, Shea-Donohue T. Th2 cytokine-induced alterations in intestinal smooth muscle function depend on alternatively activated macrophages. *Gastroenterology* 2008;135:217–225.e1.
 57. von Lampe B, Barthel B, Coupland SE, Riecken EO, Rosewicz S. Differential expression of matrix metalloproteinases and their tissue inhibitors in colon mucosa of patients with inflammatory bowel disease. *Gut* 2000;47:63–73.
 58. Zlokovic BV. The blood-brain barrier in health and chronic neurodegenerative disorders. *Neuron* 2008;57:178–201.
 59. Jung S, Aliberti J, Graemmel P, Sunshine MJ, Kreutzberg GW, Sher A, Littman DR. Analysis of fractalkine receptor CX(3)CR1 function by targeted deletion and green fluorescent protein reporter gene insertion. *Mol Cell Biol* 2000;20:4106–4114.
 60. Ferenczi S, Szegi K, Winkler Z, Barna T, Kovács KJ. Oligomannan prebiotic attenuates immunological, clinical and behavioral symptoms in mouse model of inflammatory bowel disease. *Scientific Reports* 2016;6:34132.
 61. van Rooijen N, Sanders A, van den Berg TK. Apoptosis of macrophages induced by liposome-mediated intracellular delivery of clodronate and propamidine. *J Immunol Methods* 1996;193:93–99.
 62. Egawa G, Nakamizo S, Natsuaki Y, Doi H, Miyachi Y, Kabashima K. Intravital analysis of vascular permeability in mice using two-photon microscopy. *Scientific Reports* 2013;3:1932.

Received September 28, 2020. Accepted July 2, 2021.

Correspondence

Address correspondence to: Nandor Nagy, PhD, Semmelweis University, Tuzolto st. 58, Budapest 1094, Hungary. e-mail: nagy.nandor@med.semmelweis-univ.hu; fax: (36) 1-2153064; or Allan M. Goldstein, MD, Massachusetts General Hospital, 55 Fruit Street, WRN 1151, Boston, Massachusetts 02114. e-mail: agoldstein@partners.org; fax: (617) 726-2167.

Acknowledgments

The authors thank Zsuzsanna Vidra and Anikó Csenkey for their technical assistance in histology.

CRedit Authorship Contributions

David Dora, PhD (Conceptualization: Lead; Data curation: Supporting; Formal analysis: Equal; Funding acquisition: Supporting; Investigation: Lead; Methodology: Equal; Project administration: Supporting; Resources: Supporting; Software: Supporting; Supervision: Equal; Validation: Supporting; Visualization: Equal; Writing – original draft: Equal; Writing – review & editing: Supporting)

Szilamer Ferenczi, PhD (Conceptualization: Supporting; Formal analysis: Supporting; Investigation: Equal; Methodology: Lead; Project administration: Equal; Resources: Equal; Supervision: Equal; Writing – original draft: Supporting; Writing – review & editing: Supporting)

Rhian Stavelly, PhD (Resources: Supporting; Supervision: Supporting; Writing – original draft: Supporting; Writing – review & editing: Equal)

Viktoria E. Toth, PhD (Investigation: Supporting; Methodology: Equal; Supervision: Supporting; Writing – review & editing: Supporting)

Zoltan V. Varga, PhD (Conceptualization: Supporting; Funding acquisition: Supporting; Investigation: Supporting; Project administration: Equal; Resources: Equal; Supervision: Supporting; Writing – review & editing: Supporting)

Tamas Kovacs, MSc (Formal analysis: Equal; Investigation: Supporting; Methodology: Equal; Visualization: Supporting; Writing – review & editing: Supporting)

Ildiko Bodi, PhD (Methodology: Supporting; Resources: Supporting; Supervision: Supporting)

Ryo Hotta, PhD, MD (Resources: Supporting; Supervision: Supporting)

Krisztina J. Kovacs, PhD (Funding acquisition: Supporting; Project administration: Equal; Resources: Equal; Supervision: Supporting; Writing – review & editing: Supporting)

Allan M. Goldstein, MD (Conceptualization: Equal; Funding acquisition: Equal; Investigation: Supporting; Project administration: Supporting;

Resources: Equal; Visualization: Supporting; Writing – original draft: Equal; Writing – review & editing: Lead

Nandor Nagy, PhD (Conceptualization: Lead; Funding acquisition: Lead; Investigation: Supporting; Project administration: Equal; Resources: Lead; Supervision: Supporting; Visualization: Equal; Writing – original draft: Lead; Writing – review & editing: Lead)

Conflicts of interest

The authors disclose no conflicts.

Funding

NN is supported by the Bolyai and Bolyai+ Fellowships from the Hungarian Academy of Sciences, Excellence Program for Higher Education of Hungary (FIKP), and Hungarian Science Foundation NKFI grant (124740). AMG is supported by the National Institutes of Health (R01DK103785). KJK and SF are supported by the Hungarian Science Foundation NKFI grant (124424). ZVV and VET are supported by the European Union's Horizon 2020 research and innovation program under grant agreement No 739593. ZVV is supported by the Bolyai Research Scholarship from the Hungarian Academy of Sciences.